



## Investigating the role of metals loaded on nitrogen-doped carbon-nanotube electrodes in electroenzymatic alcohol dehydrogenation

Sanath Kondaveeti <sup>a,1</sup>, Gi Dae Park <sup>b,1</sup>, Ramasamy Shanmugam <sup>a,1</sup>, Raviteja Pagolu <sup>a</sup>, Sanjay K. S. Patel <sup>a</sup>, Aarti Bisht <sup>a</sup>, Dong Rip Kim <sup>c</sup>, Yun Chan Kang <sup>d,\*</sup>, Jung-Kul Lee <sup>a,\*</sup>

<sup>a</sup> Department of Chemical Engineering, Konkuk University, 1 Hwayang-Dong, Gwangjin-Gu, Seoul 05029, Republic of Korea

<sup>b</sup> Department of Advanced Materials Engineering, Chungbuk National University, Chungdae-ro 1, Seowon-gu, Cheongju, Chungbuk 28644, Republic of Korea

<sup>c</sup> Department of Mechanical Engineering, Hanyang University, 222 Wangsimni-ro, Seongdong-gu, Seoul 04763, Republic of Korea

<sup>d</sup> Department of Materials Science and Engineering, Korea University, Anam-Dong, Seongbuk-Gu, Seoul 02841, Republic of Korea



### ARTICLE INFO

#### Keywords:

Metal alloy nanoparticle  
Carboligation  
Acetoin  
Enzyme fuel cell  
First-principle analysis

### ABSTRACT

A new enzymatic biofuel cell (EBFC) is developed using conductive metal alloy nanoparticles with carbon cloth (CC) as an immobilization support for ethanol dehydrogenase (EtDH) and formolase (FLS). Ethanol (EtOH) dehydrogenation to acetaldehyde via direct electron transfer (DET) is pursued as the first step, followed by the condensation of acetaldehyde to acetoin. Metals are deposited onto novel three-dimensional jellyfish (JF)-shaped nanoparticles ( $\text{SiO}_2\text{-NCNT-}\text{CoFe}_2$ ), where NCNT denotes “N-doped carbon nanotube”. The fabricated JF–metal–CC–EtDH bioelectrodes exhibit a variation in power generation with varying metals, with a value 37.6-fold higher than that of previously reported EBFC operations with DET for EtOH oxidation. The highest acetoin content is also found in JF–Os–CC–EtDH–FLS, attributable to faster electron uptake by the bioelectrode. First-principles calculations suggest that the d-state delocalization of metal-loaded JF particles is the cause of the enhanced catalytic activity, and it can be utilized in designing electrocatalysts.

### 1. Introduction

Fuel cells (FCs) are electrical energy-generating systems that can convert chemical energy into electrical energy. Biological fuel cells (BFCs) have attracted much attention as a renewable and sustainable energy generation technology for powering compact devices through immobilization with bioelectrogens or enzymes as principal facilitators [1]. BFCs function like conventional FCs: the organics are oxidized at the anode with the simultaneous reduction of electron acceptors (typically  $\text{O}_2$  in the air) at the cathode. BFCs that use enzymes as anode biological catalysts are called “enzymatic biofuel cells” (EBFCs). These can exploit a wide range of abundant organic compounds, such as alcohols, sugars, and fatty acids [2]. Moreover, the operation of EBFCs in ambient environments and at close to the bodily pH points is desirable. This has been sought by pursuing the bioelectrocatalysis of numerous organics [3,4].

Although enzymes are multitasking catalysts, establishing an effective electrical connection between the enzymes and electrode is not a simple task, and many researchers have explored it in the past decade. To accomplish this, redox mediators are introduced between the enzyme

and the conductive support to enhance the electrical communication between the electrode and enzyme, thereby enhancing the power output. However, redox mediators and cofactors such as nicotinamide adenine dinucleotide (NADH) in EBFCs can lead to instability, high cost, low open-circuit voltage (OCV), and washout [3,5]. Thus, research is being conducted to develop a direct electron transfer (DET)-based EBFC (DET-EBFC) with enhanced performance to increase power generation. In addition, conductive materials with a large surface area, such as carbon nanotubes (CNTs), graphene, and mesoporous carbon, are recommended for improving the power generation of bioelectrodes because they demonstrate satisfactory electrical interactions with the enzyme [6, 7]. However, the use of enzymes on carbon supports via the conventional adsorption process has several drawbacks, such as uncontrollability in the interfacial distance and weak binding, resulting in inadequate utilization of the enzyme for the desired electrochemical reactions.

The use of carbon supports with a high surface area, such as multi-walled CNTs, along with a combination of metal nanoparticles (NPs) and molecular linkers, such as polyethyleneimine (PEI), can enhance the

\* Corresponding authors.

E-mail addresses: [yckang@korea.ac.kr](mailto:yckang@korea.ac.kr) (Y.C. Kang), [jkrhee@konkuk.ac.kr](mailto:jkrhee@konkuk.ac.kr) (J.-K. Lee).

<sup>1</sup> These authors contributed equally to this work.

performance of bioelectrodes for prolonged durations [8,9]. To this end, metal NPs with higher conductivity and CNTs have been tested in FCs and are considered promising for enhancing performance [10,11]. However, these studies have been limited to simultaneous power generation and value-added product formation in EBFCs. In addition, the origin of these noble metal catalyst activities in combination with other metals is uncertain. Thus, comprehensively evaluating the structure–activity correlation of these NPs can be beneficial for identifying the empirical electrocatalytic activity of EBFCs or FCs. For instance, the d-band center values of Fe-based NPs have been correlated with electrocatalytic activity, the oxygen reduction reaction (ORR), and metal conductivity by theoretical calculations and experimental investigations, suggesting the suitability of Fe family materials for improving the ORR [12]. The electronic characteristics of metallic NPs are closely correlated with their electrocatalytic performance. Predicting the electronic structural variability in NPs can help to explore the structure–function relationship in depth. This can inform the selection of metal NPs to achieve the best EBFC performance experimentally.

Ethanol (EtOH) is commonly used as a feed at the anode with enzymes in EBFCs because of its favorable traits, such as high energy density and the possibility of production from renewable sources. These characteristics make EtOH a suitable candidate for energy transformation devices such as FCs [13]. Moreover, the continuous increase in EtOH production has led to a drastic price drop. Therefore, the focus has shifted from using it in the automobile industry as a fuel additive because of the corrosivity of engine and fuel pipelines to energy generation and value-added product formation [14]. Therefore, the use of EtOH as a feedstock in FCs can be beneficial. Nevertheless, the dehydrogenation of EtOH in FCs seems to be incomplete and restricted by the generation of end products, such as  $\text{CO}_2$ , which require further treatment [15]. Therefore, the generation of acetoin through the carboligation of acetaldehyde using FLS during EtOH oxidation in EFCs is beneficial. The EBFC anode enzyme, EtDH, dehydrogenates EtOH to acetaldehyde. Acetaldehyde is then transformed to acetoin via a carboligation reaction by FLS. During the dehydrogenation of EtOH to acetaldehyde, one proton and two electrons are generated. In the carboligation reaction, one mole of acetoin requires two moles of acetaldehyde. In addition, the cost of acetoin is 31 times higher than that of EtOH, according to global trade data, and it has a large demand in the food and chemical industries [16,17]. Therefore, acetoin is considered a potential candidate for synthesis and utilization by the U.S. Department of Energy [18].

In the present study, novel metal-deposited jellyfish (JF)-like structured particles with high conductivity were synthesized by spray pyrolysis and several simple post-treatments. The ideal physical and chemical characteristics for efficient enzyme immobilization and use as microreactors in biofuel cells were realized by these metal-deposited JF particles. An EBFC electrode was prepared by combining metal-JF and carbon cloth (CC). First-principles-based density functional theory calculations were performed to explore the general correlation between the power generation during EtOH dehydrogenation and acetoin formation using the proposed metal-JF. This unique assembly of multiple enzymes with conductive JF electrodes makes it possible to devise a novel type of EBFC for simultaneous power generation and acetoin formation.

## 2. Experimental section

### 2.1. Materials and chemicals

A H-type double-chambered EBFC with an aerated cathode was fabricated using borosilicate glass, which was used for EtOH dehydrogenation and carboligation with simultaneous power generation (Fig. S1). The CC for the anode electrode of the EBFC was purchased from fuel cell store in the USA. The enzymes for EtOH oxidation (ethanol dehydrogenase, (EtDH)) to acetaldehyde and formolase (FLS) for carboligation of acetaldehyde to acetoin were taken from *Cupriavidus*

*neocator* and *Pseudomonas fluorescens*, respectively. EtDH and FLS were cloned, expressed, and purified as previously described [16]. Potassium hexacyanoferrate(II) trihydrate ( $\text{K}_4[\text{Fe}(\text{CN})_6] \cdot 3\text{H}_2\text{O}$ ), branched polyethylenimine (PEI) with various molecular weights, and all other chemicals and reagents were of analytical grade, procured from Sigma-Aldrich. All reagents were prepared using 18-M $\Omega\text{cm}$  Millipore distilled water.

### 2.2. Synthesis of jellyfish-structured NPs

JF-like nanostructured NPs were produced by spray pyrolysis and several-step post-treatment processes. First, the precursor powders of  $\text{CoFe}_2\text{O}_4\text{--C}$  microspheres were directly prepared by spray pyrolysis using a spray solution containing  $\text{Co}(\text{NO}_3)_2 \cdot 6\text{H}_2\text{O}$  (0.033 M),  $\text{Fe}(\text{NO}_3)_2 \cdot 9\text{H}_2\text{O}$  (0.067 M), and citric acid (0.4 M). The spray pyrolysis system used in this study was described in the previous literature [19, 20]. The prepared precursor ( $\text{CoFe}_2\text{O}_4\text{--C}$ ) was changed to  $\text{CoFe}_2\text{O}_4@\text{SiO}_2$  using the modified Stöber method. The  $\text{SiO}_2$  coating procedures used in this study are described in detail in the SI. The obtained  $\text{SiO}_2$ -coated  $\text{CoFe}_2\text{O}_4$  microspheres were post-treated with excess dicyandiamide (DCDA) under an Ar atmosphere at 800 °C for 2 h. During the post-treatment step, the N-doped CNTs were grown inside the  $\text{SiO}_2$ -coated  $\text{CoFe}_2\text{O}_4$  hollow particles, and their continuous growth caused the  $\text{SiO}_2$ -coated  $\text{CoFe}_2\text{O}_4$  hollow particles to break, resulting in JF-like particles. The obtained JF-structured NPs were deposited by a various-metal (Fe, Os, Pt, Re, and Ru) salt-dissolved solution by a simple drop-and-dry method. After a simple post-treatment in an Ar atmosphere, metal-deposited jellyfish-structured NPs were synthesized.

### 2.3. Fabrication of electroenzymatic electrode

A CC electrode was wired using a conductive epoxy (Fig. S2) before the fabrication of the bioelectrode. The wired CC itself is hydrophobic, and it is difficult to disperse the aqueous EtOH/PEI mixture and EtDH or FLS on the electrode surface. Therefore, the CC was first sequentially sonicated in acetone, isopropyl alcohol, and DI water for 90 min each and then dried at 50 °C for 30 min. Later, the CC was heated in a KOH (3 M) solution at 80 °C for 1 h to activate the hydroxyl (OH) groups [21]. This step increased the hydrophilic nature of the CC, allowing the PEI mixture containing JF-shaped NPs (PEI-JFs) to permeate the CC support (Fig. S3). Next, the CC composed of hydroxyl groups was dipped and vortexed in 10 mL PEI-JF EtOH solutions for 3 h to establish amine functionalization. The PEI-JF mixture was prepared by dispersing 10 mg of JF-shaped NPs into EtOH-containing branched PEI (3 mg mL<sup>-1</sup>). This was followed by drying at room temperature and washing by dipping in DI water to remove unanchored components. The resulting JF-CC with PEI is an outcome of the amine (NH<sub>2</sub>) groups of PEIs and hydroxyl (OH<sup>-</sup>) groups of CC. This electrode was used for the enzyme fixation. PEI-JF-coated CC (Fig. S4) was used to immobilize EtDH (3 U) and FLS (3 U). The enzyme-fixed bioelectrodes were washed with HEPES buffer (pH 8.5, 50 mM) to remove unbound proteins. During this protein deposition process, the negatively charged EtDH and FLS in HEPES were bound to the positively charged JF-CC with the PEI electrode [3]. In the initial power generation analysis, only EtDH was used. After optimization of power generation, both enzymes (EtDH and FLS) were deposited on the bioanode for simultaneous power generation and carboligation.

### 2.4. Electrochemical characterization of the electrode

All electrochemical analyses were performed using a biologic SP150 potentiostat. The enzyme-immobilized bioelectrode, Pt wire, and Ag/AgCl (sat. NaCl) served as the working, counter, and reference electrodes, respectively. All the reported values in cyclic voltammetry (CV) and chronoamperometry (CA) were referenced against the Ag/AgCl electrode unless stated otherwise. Before the electrochemical analysis and EBFC operation, the anolyte, 15 mL of HEPES buffer (50 mM, pH

8.0), was sparged with nitrogen gas for 30 min to remove dissolved oxygen. All the electrochemical measurements were an average of multiple cycles ( $n = 3\text{--}5$ ) with calculated standard deviations. Electrochemical impedance spectroscopy (EIS) analysis was performed from 100 kHz to 10 mHz with an amplitude voltage of 10 mV. The Nyquist impedance spectra of the EIS were fitted using the Zview program. The abiotic operation for the electrochemical characterization of NPs was pursued with a glassy carbon electrode (GCE). CV and EIS were performed in a nitrogen-sparged 100 mM KCl solution containing  $\text{K}_4[\text{Fe}(\text{CN})_6] \cdot 3\text{H}_2\text{O}$  (5 mM). During the EBFC operation, metallic JFs were deposited with pretreated CC for power generation and carboligation. The biotic Tafel analysis was performed in a three-electrode system from  $-0.2$  to  $+0.8$  V (versus Ag/AgCl). The electrochemical analysis was further computed from Eqs. (S1–S6) to evaluate the EBFC performance.

## 2.5. Construction and operation of EBFC

A square NP-CC-EtDH enzymatic electrode was used as a bioanode in the EBFC, along with a platinum wire as the cathode (Fig. S1). The anode and cathode were separated using a pretreated proton exchange membrane (PEM; Nafion-117) [22]. Membrane pretreatment was performed as described in Section 2.1 of Supplementary Information. A control fuel cell with and without an enzyme was also examined for background power generation.

## 2.6. Analytical methods for the quantification of the substrate and the products in EBFC

The substrate and product concentrations were determined by Gas chromatography (GC), as described in earlier studies [16]. In brief, EtOH, acetaldehyde, and acetoin concentrations were quantified using GC (Agilent GC9860, CA, USA) equipped with Supelco  $\beta$ -DEX<sup>TM</sup> 120 chiral columns (30 m length  $\times$  0.25 mm inner diameter) and flame ionization detector. The carrier gas was  $\text{N}_2$  at a flow rate of 1.2 mL/min. The detector and injector port temperatures were fixed at 245 °C and 215 °C, respectively. The column temperature was held at 50 °C for 2 min, which was then gradually increased up to 180 °C at a rate of 15 °C/min. Additionally, acetoin was quantified by the Voges–Proskauer (VP) reaction, as previously described [16].

## 2.7. First-principles calculations of JFs

A plane-wave self-consistent field (PWScf) framework was implemented in Quantum Espresso 6.4.1 software for structure optimization, calculation of energies, and determination of the electronic structure properties of the control JF and metal-deposited JFs [23]. The generalized gradient approximation method with the Perdew–Burke–Ernzerhof function was used to treat the exchange-correlation energy. The Kresse–Joubert projector augmented wave pseudopotential was used to treat the ionic cores of the atoms. To achieve better convergence, a threshold value of 0.01 eV Å<sup>-1</sup> and  $10^{-5}$  eV was applied for the force of action on an atom and electronic energy, respectively. Kinetic energy and cutoff energies of 40 and 320 Ry, respectively, were used to describe the wave function. A single gamma k-point was used to represent the Brillouin zone. Electron density differences and partial density of states (PDOS) were used to characterize the electronic interactions in the control and metal-deposited JF particles. Molecular docking simulations were performed using the AutoDock 4.2 [24]. SI Section 15 provides details regarding the selected models used in this study.

## 3. Results and discussion

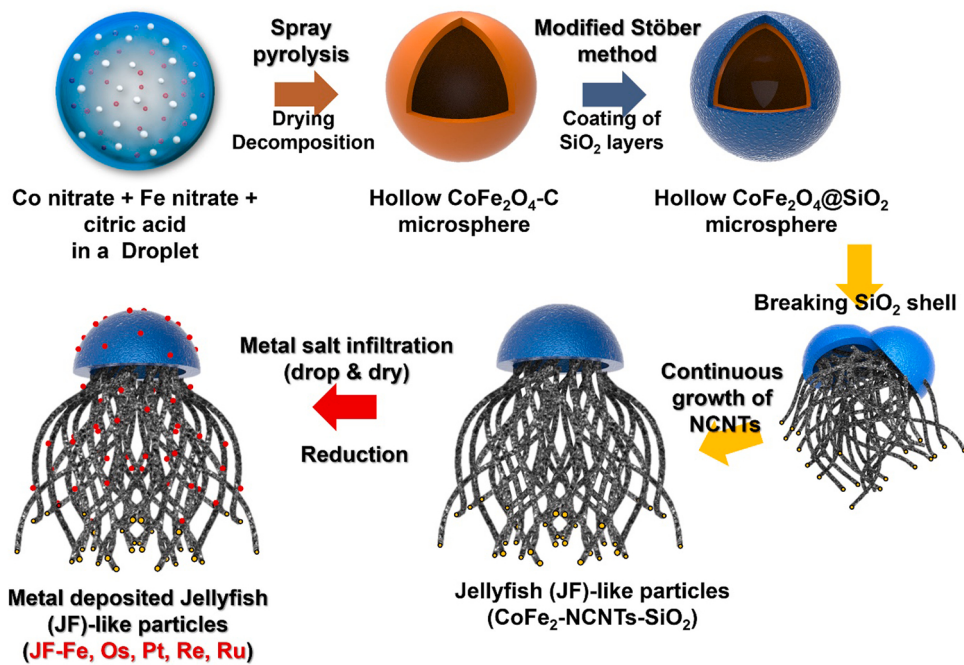
### 3.1. Synthesis and structural characterization

The synthetic procedure for the metal-deposited JF-like structured

particles is shown in Scheme 1. The precursor for the in-situ growth of N-doped CNTs (NCNTs) via a metal catalyst was prepared by simple and scalable spray pyrolysis and the modified Stöber method. The droplet, which was produced by a spray generator, contained cobalt nitrate, iron nitrate, and citric acid. Hollow-structured  $\text{CoFe}_2\text{O}_4\text{--C}$  microspheres were prepared through drying and decomposition during spray pyrolysis. Subsequently, a thin  $\text{SiO}_2$  layer was coated over  $\text{CoFe}_2\text{O}_4\text{--C}$  using the modified Stöber method. When subjected to a temperature of 800 °C, the precursor ( $\text{CoFe}_2\text{O}_4@\text{SiO}_2$ ) was reduced to CoFe<sub>2</sub> alloys, whereas excess dicyandiamide (DCDA) was decomposed to form carbon nitride gas. Because of the effect of the metal catalyst, the nitrogen-doped CNTs (NCNTs) grew uniformly toward the center as a result of the outer  $\text{SiO}_2$  layers. The continual growth of NCNTs eventually broke the outer  $\text{SiO}_2$  shell and formed JF-like structured particles. Various metal (Fe, Os, Pt, Re, and Ru) salts were dissolved in EtOH, and the dissolved solutions were coated onto the prepared JF particles. After post-treatment to decompose the metal salts, metal-deposited JF particles were obtained.

To prepare the precursor as a substrate, hollow-structured  $\text{CoFe}_2\text{O}_4\text{--C}$  microspheres with a mean size of 1.4  $\mu\text{m}$  were synthesized by spray pyrolysis, as shown in Fig. S5a and b in the Supporting Information. Using the modified Stöber method, the  $\text{CoFe}_2\text{O}_4\text{--C}$  microspheres were well coated with a thin  $\text{SiO}_2$  layer, as shown in Fig. S5c and S5d. The  $\text{SiO}_2$ -layer-coated  $\text{CoFe}_2\text{O}_4\text{--C}$  microspheres were post-treated under an Ar atmosphere with excess DCDA, resulting in the growth of NCNTs. Fig. 1a and b show the continued growth of the NCNTs with the JF particles. The high-resolution TEM image (Fig. 1c) shows that the CoFe<sub>2</sub> nanocrystals were covered with NCNTs with clear lattice fringes spaced at 0.20 and 0.34 nm apart, corresponding to the (110) and (001) crystal planes of metallic CoFe<sub>2</sub> alloy and graphitic carbon, respectively. The elemental dot mapping images (Fig. 1d) reveal broken  $\text{SiO}_2$  shells (Si and O components) and well-grown NCNTs (C and N components). The prepared JF particles were coated with various metal catalysts using a simple drop-and-dry method followed by a one-step post-treatment process (Fig. 1e–x). The low-resolution transmission electron microscopy (TEM) images of the metal-deposited JF particles showed similar morphologies to the JF-like structures. However, in the high-resolution TEM images of the metallic JF particles, (Fe, Os, Pt, Re, and Ru) nanodots were observed on the NCNT surface. In contrast, other metal nanocrystals were not observed in the bare JF particles. The high-resolution TEM image (Fig. 1g, k, o, s, and w) revealed that the clear lattice fringes spaced 0.20, 0.21, 0.21, 0.23, and 0.22 nm apart, corresponding to the (111), (101), (111), (111), and (111) crystal planes of metallic Fe, Os, Pt, Re, and Ru nanodots, respectively. The uniform distribution of the metal (Fe, Os, Pt, Re, and Ru) catalysts over JF particles was confirmed by the elemental mapping images in Fig. 1h, l, p, t, and x, respectively. Various metal (Fe, Os, Pt, Re, and Ru) signals demonstrated the successful deposition of metal nanocrystals on the JF structures.

Because the proportion of deposited metal crystals to the total JF particles was small, X-ray photoelectron spectroscopy (XPS) analysis, which is widely used as a surface-sensitive quantitative spectroscopic technique, was conducted to confirm the presence of deposited metals (Fe, Os, Pt, Re, and Ru) over JF particles. As components consisting of JF particles, the Co 2p and Fe 2p spectra were deconvoluted into fitted peaks, as shown in Figs. 2a and S6, respectively. The XPS spectra of Co 2p in Fig. 2a show that the binding energies exactly corresponded to those of the two spin orbitals of Co 2p<sub>3/2</sub> and Co 2p<sub>1/2</sub>, at 778.4 and 793.3 eV, respectively, indicating a metallic Co state [25]. The Co 2p<sub>3/2</sub> and Co 2p<sub>1/2</sub> orbital peaks at 780.1/782.5 and 795.8/797.2 eV, respectively, confirmed that the formation of the  $\text{CoO}_x$  phase was due to the easily oxidized surface of metallic Co during sample preparation for XPS analysis [25]. Fe 2p shows a similar tendency as metallic Fe (Fe<sup>0</sup> orbital peaks at 707.4 eV) and  $\text{FeO}_x$  (Fe<sup>2+</sup> and Fe<sup>3+</sup> orbital peaks at 710.3 and 713.7 eV, respectively) in Fig. S6 [26]. However, the Fe 2p, Os 4f, Pt 4f, Ru 3d, and Re 4f spectra were deconvoluted into their fitted peaks, as shown in Fig. 2b–f. The Fe 2p spectrum of the Fe-deposited JF



Scheme 1. Synthetic procedures for producing metal-deposited JF-like structured particles.

particles exhibited similar fitted peaks, corresponding to metallic Fe and  $\text{FeO}_x$  components. The Os 4f orbital peaks at 50.8 eV correspond to the metallic Os phase, as shown in Fig. 2c [27].

However, metallic Os is known to be sensitive to air oxidation and can form  $\text{OsO}_x$ , as shown by the peaks at 51.7/54.0 ( $\text{Os}^{2+}$ ) and 56.0 ( $\text{Os}^{4+}$ ) eV, respectively [27]. The Pt 4f spectrum exhibited noticeable doublet peaks at 71.2 and 74.5 eV, which correspond to Pt 4  $f_{7/2}$  and Pt 4  $f_{5/2}$ , respectively, indicating a metallic Pt state. The other fitted peaks, which are related to the partially oxidized PtO phase, were observed at 72.0 and 75.5 eV [28]. The Re 4f spectrum of Re-deposited JF showed two prominent peaks, at 40.7 and 43.3 eV, corresponding to Re 4  $f_{7/2}$  and Re 4  $f_{5/2}$ , respectively, which are relevant to the metallic Re phase [29]. The partially oxidized  $\text{RuO}_x$  phase was formed because of the easily oxidized surface of metallic Ru. The contributions attributed to the metallic Ru (280.2 and 284.4 eV) and  $\text{Ru}^{4+}$  (284.6 and 285.7 eV) species were observed in the Ru 3d<sub>3/2</sub> and Ru 3d<sub>5/2</sub> orbital XPS spectra of Ru-deposited JF [30]. The JF and JF-metal samples exhibited similar N 1s and C 1s spectra, as shown in Fig. 2g and h. The N 1s spectrum in Fig. 2g was deconvoluted into four peaks, corresponding to pyridinic N (397.9 eV), pyrrolic N (398.5 eV), graphitic N (400.6 eV), and oxidized N (403.2 eV), confirming the presence of nitrogen-doped CNTs [31]. The C 1s spectrum in Fig. 2h shows three fitted peaks. The first main peak at 284.6 eV corresponds to C—C bonds, whereas the second and third peaks, at 285.2 and 287.9 eV, correspond to C—N and C—O bonds, respectively [32].

Raman spectroscopy was used to investigate the degree of graphitization of the carbon component because the D and graphite G bands suggested disorder/defects and crystallinity of the  $\text{sp}^2$  carbon atoms, respectively [33]. The  $I_D/I_G$  value (1.06) of the JF particles suggested that the NCNTs had defects that resulted from incorporating N dopants and metal encapsulation. After metal deposition over JF particles, the  $I_D/I_G$  of the metal-deposited JF particles showed similar values, revealing that the graphitization degree of the NCNTs was preserved. The XRD patterns of JF and metal-deposited JF particles, as shown in Fig. 2j, exhibit peaks related to the  $\text{CoFe}_2$  alloy and graphitic carbon, respectively.

The  $\text{N}_2$  adsorption and desorption isotherms and Barrett–Joyner–Halenda (BJH) pore size distributions obtained for JF and metal-deposited JF particles are shown in Fig. S7. The isotherms and

pore size distribution of JF exhibited a general type II plot with an H4 hysteresis loop, indicating the presence of mesopores between the NCNT bundles; the metal-deposited JF showed the same hysteresis loop, as shown in Fig. S7a [34]. Furthermore, the BJH pore size distribution of JF and metal-deposited JF particles showed mesopores and macropores 5–100 nm in size, which were derived from the patulous tail part of the NCNTs. The rationally designed metal-deposited JF with meso- and macropores facilitated efficient enzyme immobilization as well as superior reaction as an enzymatic biofuel cell. The Brunauer–Emmett–Teller (BET) surface areas of JF, JF–Fe, JF–Pt, JF–Os, JF–Re, and JF–Ru were 144, 103, 143, 132, 142, and  $110 \text{ m}^2 \text{ g}^{-1}$ , respectively (Table S1, Supporting Information). Even the metal deposition process, mean pore volume, and pore diameter size exhibited similar values because of the small amount of deposited metal elements. Moreover, it appears that the metal deposition process does not affect the pore structure of the JFs. The as-prepared porous NPs are black, without any change in apparent color after the addition of metals such as Fe, Ru, Re, Pt, and Os on the control JF particles (Fig. S8).

### 3.2. Electrochemical characterization of NCNT-based metal-deposited JFs

The influence of NP modification by the introduction of various metals on the electrocatalytic properties was analyzed by performing cyclic voltammetry (CV) and electrochemical impedance spectroscopy (EIS) studies in a  $\text{KCl}$  (100 mM) and  $\text{K}_4[\text{Fe}(\text{CN})_6] \cdot 3\text{H}_2\text{O}$  (50 mM) solution. The electrochemical activities of JF-shaped particles and the introduction of various metals were preliminarily tested using a plain glassy carbon electrode (GCE). CV analysis was conducted, and the redox peak current is shown in Fig. S9a and b. The plain GCE exhibited lower electrochemical activity as compared to the JFs, with the smallest anodic peak current density value being  $0.052 \text{ mA cm}^{-2}$  after the deduction of the background current. In contrast, the introduction of metallic JFs led to a well-defined redox peak due to an increase in conductivity, thus implying the critical role of JFs in enhancing the electrochemical activity. From the CV analysis, it is evident that the incorporation of metals into JFs promoted electron transfer at the GCE. The redox peak currents depended on the type of metal incorporated with the JFs. Among all the metallic JFs, JF–Os–GCE exhibited the highest electrocatalytic performance (anodic current density:

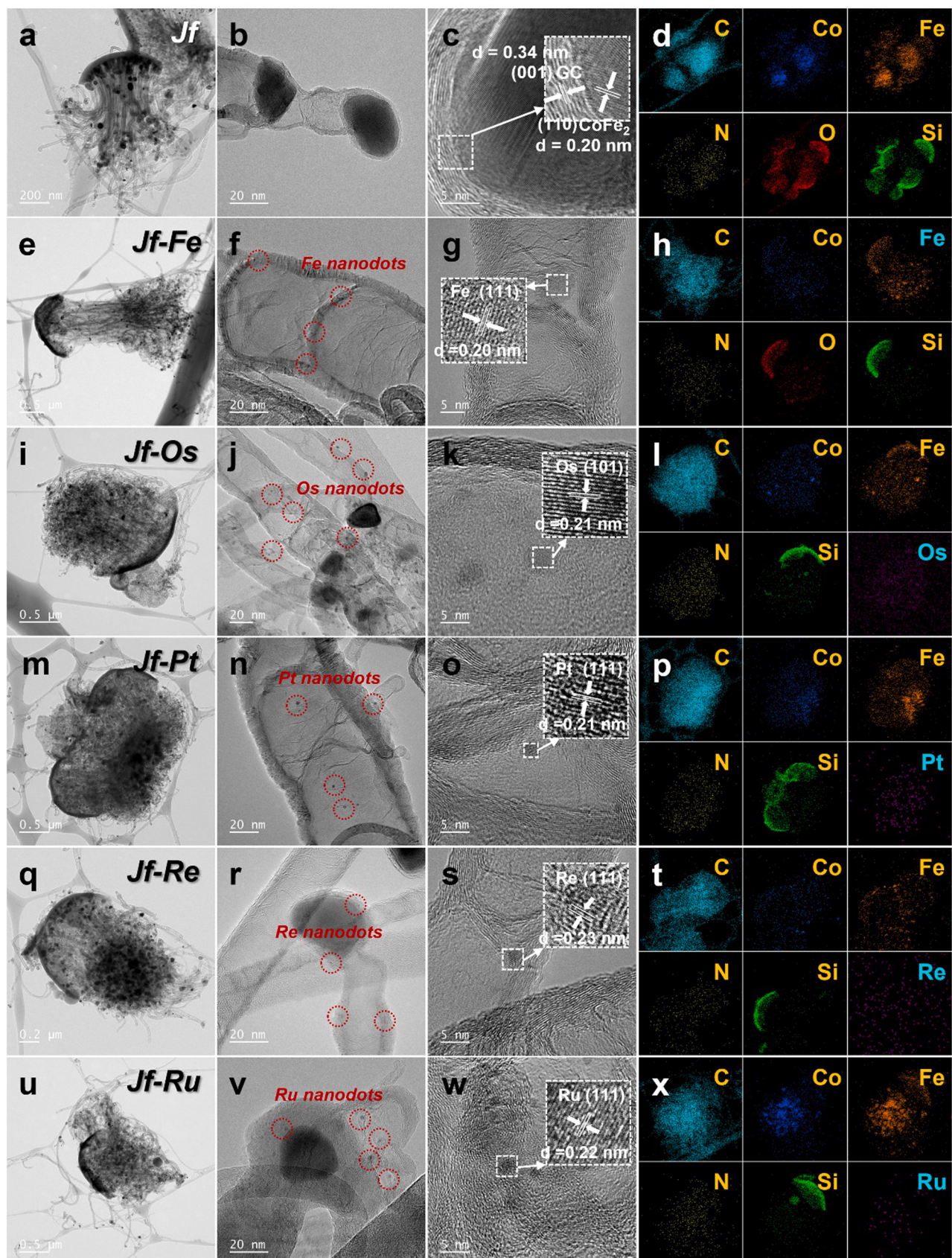


**Fig. 1.** (a,e,i,m,q,u) TEM, (b,c,f,g,j,k,n,o,r,s,v,w) high-resolution TEM, and (d,h,l,p,t,x) elemental mapping images of metal-deposited JF-like structured particles: (a-d) JF, (e-h) JF-Fe, (i-l) JF-Os, (m-p) JF-Pt, (q-t) JF-Re, and (u-x) JF-Ru.

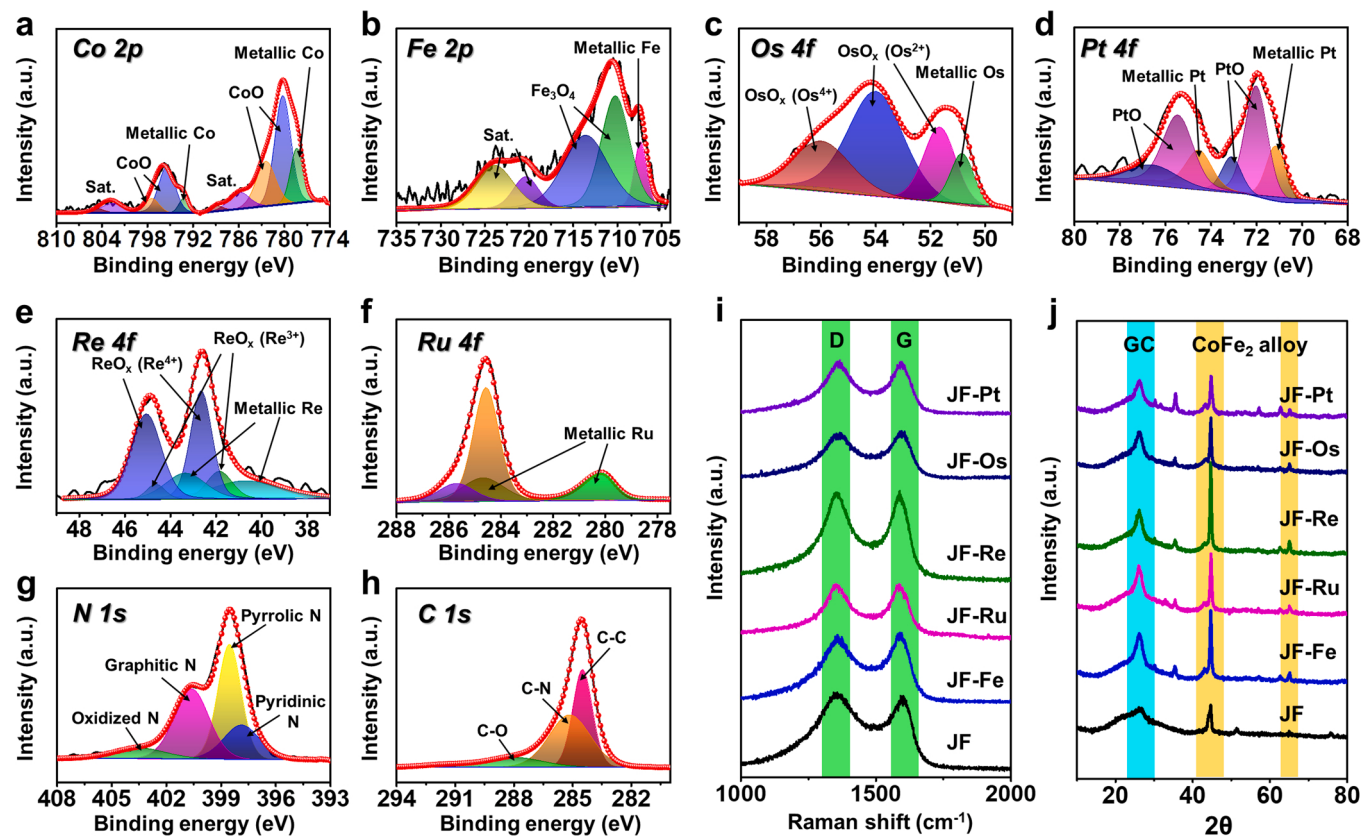


**Fig. 2.** XPS spectra (a–h), Raman spectra (i), and XRD (j) patterns of JF and metal-deposited JF: (a) Co 2p of JF and metal-deposited JF, (b) Fe 2p of JF-Fe, (c) Os 4f of JF-Os, (d) Pt 4f of JF-Pt, (e) Re 4f of JF-Re, (f) Ru 4f of JF-Ru, (g) N 1s of JF, (h) C 1s of JF, (i) Raman spectra, and (j) XRD patterns.

0.415 mA cm<sup>-2</sup>). This could be explained by the strong electronic interaction of Os with JF, which can enhance the electrochemical performance, and consequently the overall catalytic activity. The control particle (JF-GCE) exhibited an oxidative current density of 0.191 mA cm<sup>-2</sup> (Fig. S9b), which was 2.17 times smaller than that of JF-Os-GCE, hence confirming the elevated performance due to Os. The anodic peak current densities of JF-Fe-GCE, JF-Ru-GCE, JF-Re-GCE, and JF-Pt-GCE were smaller than those of JF-Os-GCE, with  $I_{pa}$  values of 0.268, 0.278, 0.335, and 0.364 mA cm<sup>-2</sup>, respectively.

To further elucidate the electrocatalytic activity, the Nyquist plot from EIS corresponding to the variation in metal alloy JFs is shown in Fig. S9c in the *Supporting Information*. Based on the EIS analysis, the presence of NPs increased the electrochemical performance and decreased the charge-transfer resistance ( $R_{ct}$ ). Among all the nonenzymatic electrodes with JFs tested, the JF-Os-GCE showed the lowest  $R_{ct}$  i.e., 363 Ω, which was consistent with the CV analysis. The  $R_{ct}$  of JF-Os-GCE was lower than that of JF-GCE (586 Ω), JF-Fe-GCE (510 Ω), JF-Ru-GCE (480 Ω), JF-Re-GCE (430 Ω), and JF-Pt-GCE (380 Ω). This is consistent with the CV data and conductivity values (Fig. S9d and e). Among the metallic JFs, JF-Os-GCE exhibited the highest catalytic performance, although its particle size and specific surface area were similar to those of other metallic JFs. The disparity in electrochemical performance mostly results from the variation in intrinsic metal-supported interactions, which play a pivotal role in influencing the power generation in EBFCs. The electrochemical performance of the JFs and metal-deposited JFs may be due to the stronger interaction between the metals and JF, resulting in increased electrocatalytic activity.

### 3.3. Ethanol dehydrogenation and power generation in EBFCs

#### 3.3.1. Characterization of EtDH immobilized on metal-deposited JFs

JF-Os-CC immobilized with EtDH (JF-Os-CC-EtDH) was initially tested for the dehydrogenation of EtOH to acetaldehyde by exploiting the DET process with EtDH at the anode. The purified EtDH and FLS showed a clear band on gel electrophoresis (SDS-PAGE) at approximately 40 and 60 kDa, respectively (Fig. S10). The attachment of EtDH was accomplished by chemical binding of the amine groups (–NH<sub>2</sub>) of cationic PEI to the carbonyl groups of EtDH in the support matrix [8]. The successful formation of C=N via the Schiff base reaction to facilitate the absorption of EtDH on the electrode surface was confirmed by Fourier transform infrared spectroscopy (FT-IR), XPS, thermogravimetric analysis (TGA), and scanning electron microscopy (SEM). Fig. S11a in the *Supporting Information* shows the FT-IR results of the EtDH, JF-Os-CC, and EtDH immobilized support matrix (JF-Os-CC-EtDH). The FT-IR spectrum of EtDH showed major peaks for amide linkage at 1640 cm<sup>-1</sup>, stretching vibrations of methylene groups at 2972 cm<sup>-1</sup>, and the presence of hydroxyl groups at approximately 3300 cm<sup>-1</sup> [35]. In the case of PEI-coated JF-Os-CC, the peak at 1069 cm<sup>-1</sup> was assigned to the Si—O bond, and that at 1248 cm<sup>-1</sup> was assigned to the –C—H bonds in CH<sub>2</sub>. The peaks between 2800 and 3000 cm<sup>-1</sup> can be assigned to the methylene groups in the PEI–JF-Os-CC network [36]. However, JF-Os-CC-EtDH showed peaks for both EtDH and JF-Os-CC, with enhanced peaks for amide and hydroxyl groups. The peaks at 1649 cm<sup>-1</sup> can be attributed to the amide group, and the peaks between 2800 and 3000 cm<sup>-1</sup> can be attributed to the dominant hydroxyl group of PEI (3300 cm<sup>-1</sup>) [36].

The valence states of the elements based on their chemical bonding in the EtDH, JF-Os-CC, and EtDH immobilized JF-Os-CC were studied by XPS, as shown in Fig. S12. Here, JF-Os-CC with PEI can interact with EtDH to form C=N. More specifically, the immobilization mechanism of

EtDH with JF–Os–CC containing PEI is explained as follows. According to the isoelectric point (5.84), the negatively charged EtDH at pH 8.5 is electrostatically attracted toward the positively charged JF–Os–CC with PEI. Later, the carbonyl groups of EtDH react with the amine groups of JF–Os–CC with PEI to form C=N bonds [8].

The Si 2p peak in JF–Os–CC and JF–Os–CC–EtDH is caused by the synthesis of NCNTs on the surface of the silica shell surface [37]. Overall, the survey scans imply that EtDH was immobilized on the surface of JF–Os–CC. To clarify the bonding between EtDH and JF–Os–CC, high-resolution C1s scan spectra were fitted using a Gaussian fitting method. Fig. S12b shows the deconvolution of a high-resolution scan of C1s spectra for EtDH, which has three chemical shifts that represent saturated or unsaturated carbon (284.1 eV), carbonyl (286.1 eV), and carboxyl (287.8 eV) groups [8]. Fig. S12c shows the deconvoluted C1s spectra for the JF–Os–CC sample. Deconvolution resulted in the following three major components. The binding energy peaks at 284.3, 285.5, and 287.4 eV are attributed to saturated or unsaturated carbon, carbon–nitrogen, and carbon–oxygen bonds, respectively [38]. Fig. S12d shows the deconvoluted C1s spectrum for JF–Os–CC–EtDH. This spectrum exhibited –C–C–/–C=C– (284.5 eV), –C–OH/–HN–C=O (285.4 eV), –C=O/–CNH<sub>2</sub> (287.9 eV), and –C–O/–N–C=O (288.7 eV) bond-related peaks [39]. After immobilization of the enzyme to the PEI-functionalized support matrix (JF–Os–CC), the appearance of –C–C–/–C=C– at 284.5 eV indicates that the JF–Os–CC is directly bonded to EtDH molecules [40]. Here, the peak corresponding to C–C bonds was predominant, and there was an

additional peak for the C–N bond. This is caused by the bonding between the carbonyl groups of EtDH and the amine groups of PEIs on the JF–Os–CC surface. Furthermore, TGA (Fig. S11b) of JF–Os–CC and EtDH-immobilized JF–Os–CC–EtDH exhibited a weight loss of 12.5%, attributable to the decomposition of the peptide chain from EtDH, thereby corroborating the successful fixation of EtDH on the support matrix.

Pristine CC electrodes consisting of carbon fibers (7.3–8.2  $\mu\text{m}$  in diameter) possess a large surface area and are suitable for improved enzyme loading. The SEM images confirm the presence of JF–Os–CC on the carbon fibers of CC, in contrast to pristine CC, and no change in the structure of CC (Fig. S13). The energy dispersive X-ray analysis (EDX) spectra (Fig. S14) show an uneven distribution of nitrogen after enzyme fixation, suggesting that the observed assembly contained EtDH and PEI.

### 3.3.2. Electrochemical characterization and optimization of modified electrodes

To further examine the electrode modifications, especially by the introduction of JF–Os onto CC and with immobilization of EtDH for dehydrogenation of EtOH to acetaldehyde, CV and EIS analyses were performed in 0.1 M HEPES buffer at pH 8.5 (Fig. 3). The Nyquist plot of the EIS spectrum based on electrode variation is presented in Fig. 3a. After the introduction of JF–Os to CC,  $R_{ct}$  decreased to 60  $\Omega$ , which is 2.6- and 4.9-fold smaller than those of JF–CC (158  $\Omega$ ) and CC (298  $\Omega$ ), respectively. After EtDH was deposited on the JF–Os–CC surface, the  $R_{ct}$  increased to 138  $\Omega$ , indicating that EtDH was well fixed on the electrode

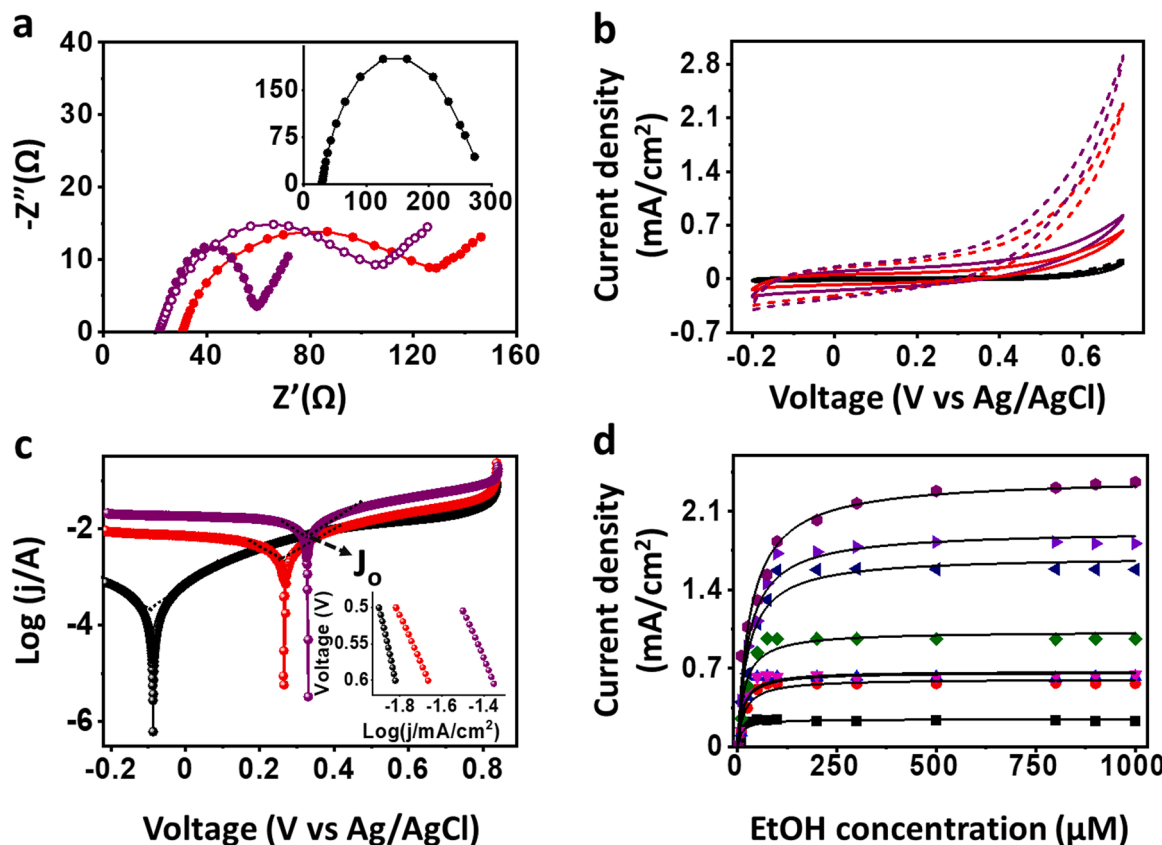


**Fig. 3.** (a) EIS of CC in inset (black circle), JF–CC (red circle), JF–Os–CC (purple circle), an enzyme immobilized JF–Os–CC (purple open circle) in oxygen-free 100 mM HEPES buffer at pH 8.5, (b) CVs of CC–EtDH (black line), JF–CC–EtDH (red line), and JF–Os–CC–EtDH (purple line) bioelectrodes in buffer at a scan rate of 10 mV/s for systems without (solid) and with (dashed) 10 mM EtOH as a substrate, (c) Tafel analysis of CC–EtDH (black circle), JF–CC–EtDH (red circle), and JF–Os–CC–EtDH (purple circle) bioelectrodes in the presence of a substrate at pH 8.5 within a potential window of –0.2–0.8 V. Inset figures show the Tafel slopes of bioelectrodes for dehydrogenation of EtOH, (d) the kinetic performance of electrodes fabricated with various metals in JF is shown for CC–EtDH (black square), JF–CC–EtDH (red circle), JF–Fe–CC–EtDH (magenta down triangle), JF–Ru–CC–EtDH (olive diamond), JF–Re–CC–EtDH (navy blue left triangle), JF–Pt–CC–EtDH (violet right triangle), and JF–Os–CC–EtDH (purple hexagon). The solid black lines in (d) are the fitting curves for Michaelis–Menten kinetics. The analysis was conducted in a nitrogen-purged buffer solution under continuous stirring.

surface of JF–Os–CC–EtDH. The oxidation current generated from dehydrogenation of EtOH by EtDH on JF–Os–CC–EtDH electrodes was found to increase at an oxidation potential of approximately 0.24 V (versus Ag/AgCl), which is similar to the theoretical redox potential of EtOH [41,42]. This oxidation potential of EtOH is notably lower than those of JF–CC–EtDH (0.28 V versus Ag/AgCl) and CC, so that the EtDH immobilized electrodes exhibit a higher electrochemical activity toward the oxidation of EtOH rather than the support CC itself (Fig. 3b). Supplementation with EtOH resulted in no significant enhancement of oxidative current generation with CC–EtDH. This indicates that DET with CC–EtDH is limited, which also suggests that the introduction of JFs plays a decisive role in interfacial electron transfer. The JF–Os–CC–EtDH (2.91 mA cm<sup>-2</sup>) electrodes in the presence of EtOH showed a 41.95% higher catalytic current compared with that of JF–CC–EtDH (2.05 mA cm<sup>-2</sup>). The introduction of metal JFs, such as JF–Os, can alter the electrochemically active surface area (ECSA), which varied from 0.16 nM cm<sup>-2</sup> for CC–EtDH to 2.36 mM cm<sup>-2</sup> for JF–Os–CC–EtDH. The JF–Os–CC–EtDH (2.91 mA cm<sup>-2</sup>) exhibits a 4.2-fold higher oxidation current than CC–EtDH (0.69 mA cm<sup>-2</sup>). Thus, the enhanced electrochemical properties and catalytic activity can be ascribed to the enhanced conductivity of the modified electrodes after introducing metal JFs onto CC; therefore, the ECSA increased. JF–Os–CC–EtDH exhibited a higher catalytic oxidative current density and  $\Gamma$  than did the other bioelectrodes. Some of the JF or JF–Os deeper in the CC may not directly interact with the electrolyte. However, the presence of JF or JF–Os demonstrated improved catalytic activity compared with that of plain CC.

To further understand EtDH fixation on the electrode (JF–Os–CC–EtDH and CC–EtDH), the immobilization yield (IY) (Table S2) and NADH generation with the immobilized electrode were analyzed. The IYs of JF–Os–CC–EtDH and CC–EtDH were 93.4% and 35.8%, respectively (Fig. S15). JF–Os–CC–EtDH exhibited 3.1 times higher NADH generation than CC–EtDH. Here, the higher IY of JF–Os–CC–EtDH is likely attributable to the stronger binding of EtDH to the support matrix. The electrochemical activity of each bioelectrode was evaluated using the Tafel slope and the charge transfer coefficient ( $\alpha$ ) using Eq. (S3). The Tafel slope of JF–Os–CC–EtDH associated with the kinetic region of EtOH dehydrogenation was 225 mV/dec (Fig. 3c). However, the slopes of CC–EtDH and JF–CC–EtDH were 604 and 421 mV/dec, respectively. The smaller Tafel slope of JF–Os–CC–EtDH indicates a rapid increase in current and suggests faster electron transfer kinetics. The  $\alpha$  values for the bioelectrodes listed in Table 1 were found to be higher for JF–Os–CC–EtDH than for other bioelectrodes, suggesting that the introduction of Os is highly favorable for EtOH dehydrogenation. Kinetics parameters, such as the electron transfer rate ( $K_{et}$ ) of each bioelectrode, were also estimated. The  $K_{et}$  values were derived from the exchange current densities ( $j_0$ ) of the Tafel plot in Fig. 3c, according to Eq. (S4). The JF–Os–CC–EtDH bioelectrode attained 2.91- and 2.15-fold higher  $K_{et}$  values than those of CC–EtDH and JF–CC–EtDH, respectively. This suggests that the electronic structure of JF–Os–CC–EtDH is suitable for reducing the potential DET energy barrier for the enzyme to dehydrogenate EtOH. The larger  $K_{et}$  value for

JF–Os–CC–EtDH is conducive for faster DET between the EtDH and the anode. The accelerated DET with JF–Os–CC–EtDH is due to an increase in the d-state delocalization electronic energy level of Os in JFs (detailed discussion provided in Section 3.3.5).

The increase in the oxidation current with the JF–Os–CC–EtDH electrode occurred when EtOH was added (Fig. S16a). It followed Michaelis–Menten kinetics and exhibited substrate saturation at 1 mM (Fig. 3a). The saturated catalytic current density ( $j_m$ ) and turnover number ( $k_{cat}$ ) varied with changes in the electrode material, as summarized in Table 1 and Table S3 in the Supporting Information. Further investigations, with changes in the molecular weight of PEI, duration of enzyme fixation, pH, ionic strength, and temperature, were also conducted (Fig. S16c–f). The performances of the enzymatic electrodes with variations in metals in the JF are compared in Fig. 3d. The  $j_m$  values of JF–Os–CC–EtDH were 3.98- and 9.9-fold higher than those of JF–CC–EtDH and CC–EtDH, respectively. The highest  $k_{cat}$  was also achieved with JF–Os–CC–EtDH, as shown in Table 1. The  $k_{cat}$  of JF–Os–CC–EtDH was found to be 3.9 and 9.4 times higher than those of JF–CC–EtDH and CC–EtDH, respectively. The higher  $j_m$  and  $k_{cat}$  can be attributed to the high conductivity of the metal JF, which improves electron transfer. The  $j_m$  and  $k_{cat}$  values of the bioconjugated electrodes followed a similar trend in the electrochemical CV, with good correlation. The order of  $j_m$  and  $k_{cat}$  for various metal JF electrodes was JF–Os–CC–EtDH > JF–Pt–CC–EtDH > JF–Re–CC–EtDH > JF–Ru–CC–EtDH > JF–Fe–CC–EtDH > JF–CC–EtDH > CC–EtDH.

EtDH was immobilized onto the electrode containing JF–Os–CC using PEI with molecular weights varying from 800 g mol<sup>-1</sup> to 75,000 g mol<sup>-1</sup> (Fig. S16b). The optimum electrochemical activity was that of the bioelectrode with branched PEI with a molecular weight of 25000 g mol<sup>-1</sup>. PEI with a low molecular weight (800 and 1500 g mol<sup>-1</sup>), compared with PEI with a larger molecular weight, is known to impair the immobilization strength of NPs and enzymes, which leads to a decrease in the current response (Table S4) [43]. To determine the absorption behavior of EtDH on the JF–Os–CC electrode, the catalytic current after different intervals of EtDH incubation was observed (Fig. S16c). A sharp rise in catalytic current was noted in the first 15 min of incubation, and stabilization of the catalytic current, with a negligible increase, was observed after 120 min of incubation. The EtDH-conjugated electrodes exhibited the highest activity at pH 8.5, which is the optimal pH for the free enzyme reaction (Fig. S16d) [16]. An increase in current density occurred with an increase in buffer concentration up to 75 mM, and there was no significant increase in current density at an ionic strength of 100 mM (Fig. S16e). Therefore, the remaining experiments were performed using a 100 mM buffer at pH 8.5. The influence of temperature (4, 30, and 60 °C) on JF–Os–CC–EtDH was estimated by observing the current generation during EtOH oxidation (Fig. S16f). An increase (3.3 times) in oxidative current occurred with an increase in temperature from 4° to 30°C. The increase in the current density may be related to the increase in EtDH activity at the optimal temperature (30 °C). Further bioelectrocatalytic measurements were performed at an optimized pH of 8.5, using 100 mM buffer at 30 °C.

### 3.3.3. Bioanodes in EBFC for power generation

The dehydrogenation of alcohol to aldehyde with simultaneous electricity generation by EtDH is the first step in the production of acetoin from EtOH. The EtDH-immobilized electrodes with JF and metal JFs were exploited as bioanodes in the EBFC and paired with a commercial Pt catalyst as the cathode (Fig. 4a). In a two-compartment fuel cell, EtOH dehydrogenation by EtDH and O<sub>2</sub> reduction by Pt were separated by a pretreated proton exchange membrane. As illustrated in Fig. 4a, the EtDH-immobilized metal JFs dehydrogenate EtOH at the anode by simultaneously releasing electrons and protons. These electrons transferred to the cathode, where they combined with O<sub>2</sub> from the air to form water. The EtDH-immobilized JF–Os–CC–EtDH exhibited excellent electrocatalytic oxidation of EtOH without any apparent deactivation. Simultaneously, the cathode was operated in a continuous

**Table 1**  
Electrochemical and kinetic performance parameters of various EtDH-immobilized electrodes for dehydrogenation of EtOH.

Parameter	Electrode	Tafel slope (mV/dec)	$\alpha$	$j_0$ (A cm <sup>-2</sup> )	$K_{et}$ (cm s <sup>-1</sup> )	$J_m$ (mA cm <sup>-2</sup> )	$k_{cat}$ (s <sup>-1</sup> )
CC–EtDH	604	0.05	$8.20 \times 10^{-5}$	$8.49 \times 10^{-9}$	0.246	0.17	
JF–CC–EtDH	421	0.08	$1.19 \times 10^{-4}$	$1.14 \times 10^{-8}$	0.601	0.40	
JF–Os–CC–EtDH	225	0.13	$2.38 \times 10^{-4}$	$2.46 \times 10^{-8}$	2.390	1.60	

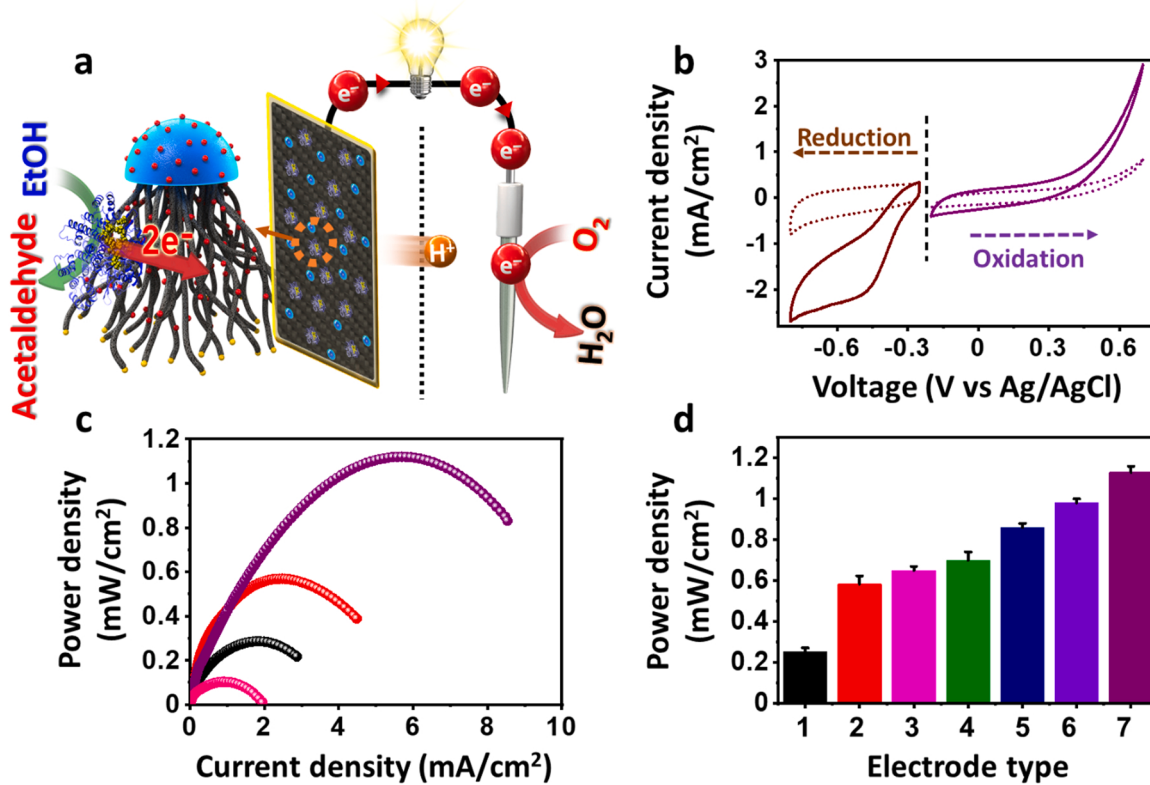


**Fig. 4.** (a) Schematic of electron transfer route from enzyme to electrode and electrode redox reactions in the fabricated two-compartment EtOH/O<sub>2</sub> EBFC, (b) CV scan of JF-Os-CC-EtDH bioanode under turnover (purple solid line), nonturnover conditions (purple dotted line), Pt wire abiotic cathode under N<sub>2</sub> (brown dotted line), and atmospheric O<sub>2</sub> from air sparging (brown solid line) with a scan rate of 10 mV/s, (c) Power density profiles of two-chamber EtOH /O<sub>2</sub> EBFC with blank (pink circle), CC-EtDH (black circle), JF-CC-EtDH (red circle), and JF-Os-CC-EtDH (purple circle), (d) summarized power density of the EtOH /O<sub>2</sub> EBFC as a function of the bioelectrode type under turnover conditions. CC-EtDH (1, black bar), JF-CC-EtDH (2, red bar), JF-Fe-CC-EtDH (3, magenta bar), JF-Ru-CC-EtDH (4, olive bar), JF-Re-CC-EtDH (5, navy blue bar), JF-Pt-CC-EtDH (6, violet bar), and JF-Os-CC-EtDH (7, purple bar). Anode chamber was supplemented with 100 mM EtOH (HEPES buffer: pH 8.5), and cathode solutions were continuously sparged with atmospheric O<sub>2</sub>.

aeration mode for power generation. An increase in the cathodic reduction current was observed with the provision of air to the cathode chamber of the EBFC (Fig. 4b). The cathode reduction peak of O<sub>2</sub> was observed at  $-0.48$  V (versus Ag/AgCl) using a Pt wire as an electrode. This O<sub>2</sub> reduction facilitates efficient operation of the EBFC for redox power generation.

Furthermore, the JF-Os-CC-EtDH bioelectrode as an anode in EtOH/O<sub>2</sub> EBFCs for maximum power generation was investigated through polarization analysis. The maximum power densities ( $P_{max}$ ) of the different bioelectrodes are shown in Fig. 4c. The bioconjugated JF-Os-CC-EtDH exhibited a  $P_{max}$  of  $1.13$  mW cm<sup>-2</sup> (Table S5). The control system using CC without EtDH exhibited a  $P_{max}$  of only  $0.09$  mW cm<sup>-2</sup>. EtDH catalyzes the dehydrogenation of EtOH by increasing the oxidation current. Therefore, the presence of EtDH on the anode presumably enhanced the  $P_{max}$  values. The EBFC operation with JF-CC-EtDH and CC-EtDH exhibited maximum  $P_{max}$  values of  $0.585$  and  $0.240$  mW cm<sup>-2</sup>, respectively. The  $P_{max}$  with JF-Os-CC-EtDH was  $1.93$ - and  $4.67$ -fold higher than those with JF-CC-EtDH and CC-EtDH electrodes, respectively (Table S5). The  $P_{max}$  data for all the electrodes (Figs. 4c and S17a) obtained from the EBFC showed a variation in behavior (Fig. 4d), as observed by the catalytic current ( $J_m$ ) results, confirming the elevated performance of the JF-Os-CC-EtDH anode compared with the other metal JF-fixed anodes. The trend of  $P_{max}$  with all the bioelectrodes tested (Fig. 4d) is as follows: JF-Os-CC-EtDH ( $1.13$  mW cm<sup>-2</sup>)  $>$  JF-Ru-CC-EtDH ( $0.976$  mW cm<sup>-2</sup>)  $>$  JF-Re-CC-EtDH ( $0.859$  mW cm<sup>-2</sup>)  $>$  JF-Ru-CC-EtDH ( $0.692$  mW cm<sup>-2</sup>)  $>$  JF-Fe-CC-EtDH ( $0.642$  mW cm<sup>-2</sup>)  $>$  JF-CC-EtDH ( $0.581$  mW cm<sup>-2</sup>)  $>$  CC-EtDH ( $0.24$  mW cm<sup>-2</sup>). The highest  $P_{max}$  with JF-Os-CC-EtDH may result from the use of metal JFs with high d-state

delocalization, such as Os, which facilitates a high electron sink between the enzyme and anode (detailed discussion provided in Section 3.3.5). In the present study, metals such as Os, Pt, Re, Ru, and Fe possessing a higher d-state delocalization promoted a higher  $P_{max}$ . We observed a strong relationship between metal (Os, Pt, Re, Ru, and Fe) d-state delocalization, leading to increased  $P_{max}$ . The maximum  $P_{max}$  observed in the present study with JF-Os-CC-EtDH was also compared with those from other studies. It was found to be 7- to  $37.6$ -fold higher than that in other enzymatic DET studies using EtOH as a substrate (Table S6).

In addition, polarization analysis was performed to test the stability of the bioelectrode with CC-EtDH and JF-Os-CC-EtDH. Because the highest value of  $P_{max}$  was observed with JF-Os-CC-EtDH, the stability analysis was performed with JF-Os-CC-EtDH as a selective system with CC-EtDH as a control. JF-Os-CC-EtDH exhibited a  $P_{max}$  decrease of  $21\%$  during repetitive operation and storage in refrigerated buffer at  $4$  °C (Fig. S17b). The larger decrease in  $P_{max}$  values with CC-EtDH (71%) can be attributed to the poor binding of EtDH to CC, thereby proving the superiority of JF-Os-CC-EtDH as a bioelectrode for EtDH immobilization. During the first week of stability analysis, a maximum decrease of  $5.4\%$  in  $P_{max}$  was observed with CC-EtDH. For JF-Os-CC-EtDH, a maximum decrease of  $0.1\%$  and  $3.5\%$  in  $P_{max}$  was observed after the first and third weeks of operation, respectively. Here, the significant enhancement in  $P_{max}$  and storage stability with JF-Os-CC-EtDH in comparison with CC-EtDH in EtOH/O<sub>2</sub> EBFC can be attributed to the porous metal alloy structure of JFs, which enables stronger binding of EtDH. Fig. 4c and d show the power densities of the EtDH electrodes depending on the presence of JF and the existing metal.

During power generation, the accumulation of the maximum number

of electrons from the dehydrogenation of EtOH is desirable for achieving a higher current density. For instance, two electrons can theoretically be collected from EtOH dehydrogenation to acetaldehyde. Accordingly, all bioconjugated electrodes were assessed for their bioelectro-oxidation profiles. The EtDH-immobilized anode during EtOH dehydrogenation for 6 h revealed that the presence of metal JFs, such as JF-Os-CC-EtDH, is highly conducive for EtOH dehydrogenation, unlike a system without metals (plain CC) (Fig. S17c, Supporting Information). As with the polarization results (Fig. 4c), JF-Os-CC-EtDH was the most active for EtOH dehydrogenation. The resulting chronoamperometric current density trend at +0.2 V for EtDH catalyzed EtOH dehydrogenation is based on enzymatic polarization analysis. It also reveals that the presence of EtDH along with the metal alloy matrix of JFs plays a crucial role in EtOH dehydrogenation. Notably, the blank sample (plain CC) did not exhibit any products after 6 h of reaction (Table S5). The CC-EtDH generated 15.5 mM acetaldehyde from 100 mM EtOH. However, the acetaldehyde concentration increased by 1.97-fold (30.2 mM) and 5.17-fold (80.2 mM) for JF-CC-EtDH and JF-Os-CC-EtDH, respectively. This indicates the supportive contribution of metal JFs to oxidative reactions. The calculated Faradaic efficiency (FE) based on the charge passed during EtOH dehydrogenation (Fig. S17c) and the charge computed based on acetaldehyde formation ranged from 48% to 78% with the incorporation of metallic JFs. This improved performance with JF-Os-CC-EtDH indicates efficient dehydrogenation of EtOH with an increase in FE of 61% and 37%, in comparison with CC-EtDH and

JF-CC-EtDH, respectively. This demonstrates the influence of Os with higher electron uptake from EtDH during the dehydrogenation of EtOH and the contribution of generated electrons for power generation in EtOH/O<sub>2</sub> fuel cells. Thus, the proposed EBFC with metal JFs collects two electrons from one molecule of EtOH and allows the carboligation of acetaldehyde to acetoin.

### 3.3.4. Carboligation of ethanol to acetoin in EBFC

Finally, a novel artificial carboligative system was developed to convert EtOH to acetoin in the EBFC anode. In EBFCs, externally supplemented regenerative systems, such as coenzymes (NADH) and mediators, have been used. However, in this EBFC, EtOH is first dehydrogenated by EtDH to generate acetaldehyde without relying on a coenzyme. Later, acetaldehyde underwent a condensation reaction to generate acetoin by FLS (Fig. 5). In general, the enzymatic cascade reaction of EtOH to acetoin requires an additional NADH cofactor as an electron acceptor, costing approximately 3000 USD bulk price per mol, which is expensive for large-scale operations and stoichiometrically limited [44,45]. Therefore, cofactor regeneration, such as the use of NADH oxidase with oxygen as a terminal electron acceptor, is necessary for practical large-scale applications. However, this adds to the supplementary operational costs for the synthesis of additional enzymes and the supply of air (O<sub>2</sub>). Based on the approximate bulk price of osmium chloride (5813 USD bulk price per mole), the average cost for the bulk synthesis of JF-Os is 0.15 USD per gram [46]. Even though the price of

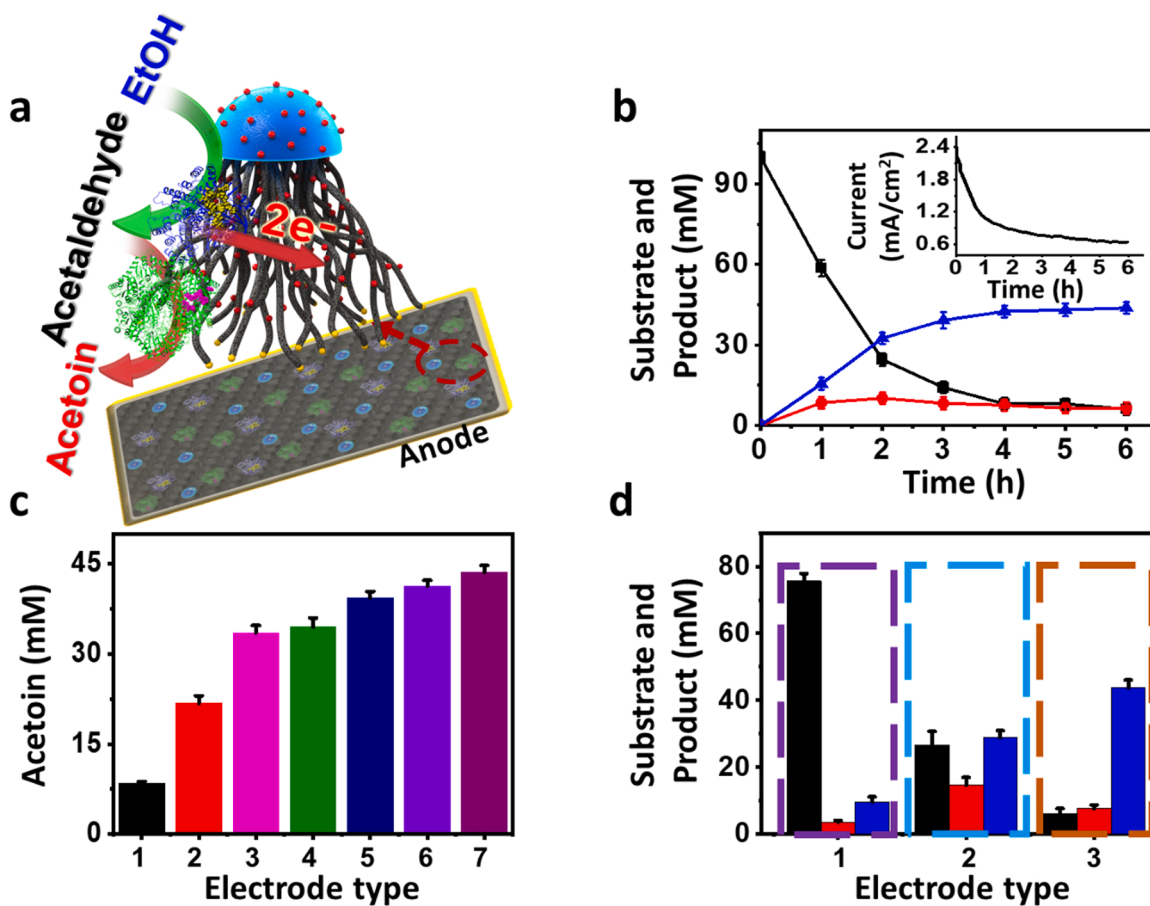


**Fig. 5.** Enzymatic biofuel cell anode for power generation and carboligation of EtOH: (a) schematic of EtOH dehydrogenation to acetaldehyde and carboligation to acetoin at the anode of EBFC, (b) time profile of acetoin generation by consuming 100 mM EtOH (black squares) as a substrate, acetaldehyde (red circle), and acetoin (blue triangle), inset points the chronoamperometric current generation observed during acetoin production in EBFC, (c) summarized acetoin generation in EtOH/O<sub>2</sub> EBFC with variation in bioelectrode type under turnover conditions. CC-EtDH-FLS (1, black bar), JF-CC-EtDH-FLS (2, red bar), JF-Fe-CC-EtDH-FLS (3, magenta bar), JF-Ru-CC-EtDH-FLS (4, olive bar), JF-Re-CC-EtDH-FLS (5, navy blue bar), JF-Pt-CC-EtDH-FLS (6, violet bar), and JF-Os-CC-EtDH-FLS (7, purple bar), (d) the residual EtOH (black bar), intermediate acetaldehyde (red bar) and acetoin (blue bar) observed in EBFC with CC-EtDH-FLS (1, purple box), JF-CC-EtDH-FLS (2, light blue box), and JF-Os-CC-EtDH-FLS (3, orange box).

Pt (6552 USD bulk price per mole) is higher, JF–Os exhibits better electrochemical activity. Therefore, using solid supports, such as a JF–Os–CC electrode without cofactors, seems beneficial for scaling up the enzymatic process. Thus, the EBFC constructed in the present study was found to be beneficial in terms of power generation with simultaneous value-added product formation over earlier enzymatic systems that depend on the regenerative mechanism.

In this study, two methods (simultaneous and sequential) of coimmobilization of EtDH and FLS onto the electrodes were used for acetoin generation (Fig. S18). During simultaneous immobilization, both EtDH and FLS were immobilized for 3 h, whereas EtDH was immobilized for 2 h in sequential immobilization, followed by FLS. Better performance in terms of enzyme immobilization yield and acetoin generation was obtained with sequential immobilization (Fig. S18a). During sequential immobilization, the maximum acetoin generation was 41.3 mM, with a yield of 82.6%. With simultaneous immobilization, the acetoin generation and yield were 35.6 mM and 71.2%, respectively. A 5.4-fold lower acetoin generation (7.64 mM) was observed with the use of EtDH and FLS as free enzymes in the anode solution. Without FLS, no acetoin generation was recorded.

It was presumed that the variance in acetoin generation in simultaneous and sequential immobilization processes resulted from a disparity in enzyme fixation during immobilization. In this regard, a quartz crystal microbalance (QCM) analysis was performed, facilitating the real-time analysis of mass changes at the picogram level (Fig. S18b) [47]. The mass of the enzyme adsorbed onto the QCM sensor was directly reflected by the variation in frequency ( $\Delta f$ ), thereby identifying an optimal coimmobilization strategy. The individual immobilization of EtDH and FLS exhibited  $\Delta f$  values of -46.69 and -123.1 Hz, respectively (Fig. S18b). The higher  $\Delta f$  change with FLS (238 kDa) is due to the large molecular mass compared with EtDH (81.3 kDa). Correspondingly, the change in  $\Delta f$  during the simultaneous immobilization ( $\Delta f = -128.3$  Hz) of EtDH and FLS was similar to the immobilization of FLS alone (-123.1 Hz). This might be due to the higher immobilization of larger enzymes, such as FLS, on the support matrix in comparison with smaller enzymes, such as EtDH. To evaluate this, two methods of sequential immobilization were conducted: i) immobilizing FLS followed by EtDH immobilization and ii) immobilizing EtDH followed by FLS immobilization. During the sequential immobilization of FLS followed by EtDH immobilization, a stable FLS  $\Delta f$  (-130.5 Hz) was recorded. After stabilization of  $\Delta f$  at 3.2 h, EtDH was immobilized onto the QCM sensor, and no significant changes in  $\Delta f$  (-132.9 Hz) were noted. This indicates that immobilization of bulkier enzymes at the start of the immobilization process limits the surface availability and entry of smaller enzymes on the support matrix. On the contrary, the efficient immobilization of both EtDH and FLS was achieved by the sequential immobilization of smaller enzymes, such as EtDH, followed by immobilization of FLS. EtDH was initially immobilized onto the QCM sensor in this sequential immobilization process, exhibiting a  $\Delta f$  of -45.25 Hz. After a stabilized  $\Delta f$  was observed at 2.8 h, FLS was immobilized onto the QCM sensor. FLS Immobilization through this sequential immobilization approach resulted in a significant increase in  $\Delta f$  (-125.3 Hz). The frequency change shows that the simultaneous coimmobilization strategy promotes the immobilization of larger enzymes such as FLS onto the support matrix rather than smaller enzymes such as EtDH. The sequential coimmobilization strategy enables the efficient immobilization of both smaller enzymes, such as EtDH (Table S7), and bulkier enzymes, such as FLS. Moreover, the JFs are porous, restricting the entry of smaller enzymes such as EtDH and favoring the immobilization of larger enzymes such as FLS during simultaneous immobilization. In the sequential coimmobilization strategy, the smaller enzyme still offers a surface available and entry for bulkier enzyme immobilization on the support matrix after the initial immobilization. Therefore, further experiments were conducted through a sequential coimmobilization strategy by immobilizing EtDH, followed by FLS immobilization onto the support matrix.

The amount of immobilized enzyme was quantified using FPLC analysis with a size-exclusion column. Thus, it is plausible to measure the enzyme content in the supernatant after immobilization, making it possible to calculate the amount of EtDH and FLS immobilized individually (Fig. S18c). Sequential immobilization resulted in EtDH and FLS IYs of 93.4% and 92.4%, respectively. With simultaneous immobilization, the EtDH and FLS IYs were 15.8% and 85.6%, respectively (Table S7). The higher immobilization of EtDH during sequential immobilization agrees with the QCM data, in which a significant change in  $\Delta f$  was found in comparison with simultaneous immobilization. Additionally, confocal laser scanning electron microscopy (CLSM) analyses were performed to visualize the distribution of enzymes in the support matrix (Fig. S18d and e). In CLSM analysis, coimmobilization through a sequential immobilization process indicated an efficient distribution of both EtDH and FLS onto the electrodes. However, through the simultaneous immobilization process, the immobilization of EtDH was noted to be lower than that of FLS.

The EtDH-and FLS-immobilized anode electrodes for current generation and carboligation are shown in Fig. 5a. On the anode, EtOH is dehydrogenated to acetaldehyde and converted to acetoin by FLS as the final product, forming a novel carboligative EBFC with simultaneous current generation. To test the viability of EBFCs for value-added product formation, acetoin generation from the oxidation of EtOH was examined using JF–Os–CC–EtDH (Fig. 5b). After 6 h of electroenzymatic reaction, the anolyte showed a maximum acetoin generation of 43.6 mM with a yield of 87.2%, indicating the possibility of upgrading EtOH with simultaneous current generation. The substrate EtOH was rapidly dehydrogenated with 8.1 mM residual EtOH in the anolyte after 6 h. The intermediate acetaldehyde concentrations increased to 10.1 mM during the initial 2 h of reaction and then decreased to 6.5 mM at 6 h. As shown in Fig. 5c, the operation of EBFC with CC–EtDH–FLS exhibited a minor acetoin generation of 8.5 mM from 100 mM EtOH after 6 h, with an acetoin yield of 16.9%. The acetoin concentrations were 2.56- and 5.12-fold lower than those of JF–CC–EtDH–FLS and JF–Os–CC–EtDH–FLS, respectively. The trend of acetoin generation was similar to that observed in EBFC polarization analyses. This indicates that the use of porous metal alloy JFs can be beneficial for product formation.

Furthermore, the product distribution (Fig. 5d) of the bioelectrodes was evaluated after 6 h of reaction for carboligation. CC–EtDH–FLS exhibited a high amount of residual EtOH (75.6 mM). However, the JF–CC–EtDH–FLS and JF–Os–CC–EtDH–FLS exhibited lower residual EtOH, with concentrations of 26.5 and 6.1 mM, respectively. This suggests that the difference in acetoin production is mostly caused by the variation in the electrode materials, which act as an electron sink. Accordingly, the influence of EtOH concentration (100–700 mM) on acetoin generation with JF–CC–EtDH–FLS (Fig. S19b) and JF–Os–CC–EtDH–FLS (Fig. S19c) were analyzed. With the increase in substrate concentration using JF–CC–EtDH–FLS and JF–Os–CC–EtDH–FLS, acetoin production increased. Similarly, intermediate acetaldehyde accumulation increased with a decrease in the theoretical yield. The maximum acetoin concentration (201.2 mM) was observed at a substrate concentration of 700 mM with JF–Os–CC–EtDH–FLS, thereby exhibiting a theoretical yield of 57.1%. The JF–CC–EtDH–FLS, however, exhibited a maximum acetoin concentration of 139.1 mM at an EtOH concentration of 700 mM, with a theoretical yield of 39.7%. No significant enhancement of acetoin generation was observed with a further increase in substrate concentration. The accumulation of acetaldehyde by increasing the substrate concentration indicates that FLS restricts acetoin production. Furthermore, because acetoin is widely used in the food industry, an acute toxicity analysis of JFs with *Vibrio fischeri*, a bioluminescent marine bacterium (Table S8), was conducted. No significant differences in acute toxicity values were observed for any of the tested JFs. This suggests that the alteration of JFs with additional metals did not alter biocompatibility. The control JF exhibited EC<sub>50</sub> values of 1022 and 988  $\mu\text{g mL}^{-1}$  after incubation for 15 and 30 min, respectively. The EC<sub>50</sub> values for JF–Os were 1016 and 981  $\mu\text{g mL}^{-1}$  after 15 and 30 min of incubation, respectively.

Fig. S20 shows the presumed reaction mechanism of EtDH and FLS cascade at the EBFC anode. EtDH is an oxidoreductase that can act as an alcohol dehydrogenase (ADH), with  $\text{Fe}^{2+}$  as the metal center. Therefore, the reaction mechanism of EtDH is presumed to be similar to that of the ADH-catalyzed EtOH oxidation. However, the reaction mechanism of FLS has not yet been discussed in the literature. Based on the homology modeling of EtDH, it is obvious that the metallic center  $\text{Fe}^{2+}$  is in coordination with His-270, His-284, His-205, and Asp-201 and can hold the OH group of EtOH at the active site. Here, the involvement of the proton relay network facilitates the deprotonation of EtOH at the active site and oxidizes it to form acetaldehyde by the consecutive generation of two electrons and one proton. These electrons are used at the anode for power generation. The generated acetaldehyde is then used as a substrate by FLS for carboligation. The GC analysis reveals a racemic acetoin formation (3 S)-acetoin and (3 R)-acetoin) from acetaldehyde. Additionally, varying amounts of Os (between 0.25 and 1.0 wt%) were loaded in the JF, and variation in electric conductivity and acetoin generation was assessed. Increasing the Os loading in the JF led to an increase in electronic conductivity. The JF loaded with 0.25 wt% Os exhibited a conductivity of  $4.31 \times 10^3 \text{ S m}^{-1}$ . The conductivity increased up to  $12.1 \times 10^3 \text{ S m}^{-1}$  for the JF loaded with 1.0 wt% Os (Fig. S21). This was not significantly different from the conductivity of 0.5 wt% of JF ( $11.2 \times 10^3 \text{ S m}^{-1}$ ). Since Os is a rare and expensive metal, it can be concluded that it is preferred to be combined with the JF structure in minimal amounts. Therefore, the JFs loaded with 0.5 wt% Os are the optimal. Moreover, the measured electrical conductivity

correlates with the acetoin generation noted in the EBFC operation. After one hour of EBFC operation with a variation in Os loading of 0.2, 0.5, and 1.0 wt% of JF, the acetoin concentration was 6.92, 15.5, and 18.6 mM, respectively.

### 3.3.5. Correlation between d-state delocalization and electrocatalytic performance

Plane-wave self-consistent field first-principles calculations on different catalysts built on cluster models were performed to explore the effect of various metals on the electrocatalytic activity. According to the EBFC performance, the addition of metals such as Fe, Ru, Re, Pt, and Os to JFs increased power generation and acetoin formation. The appropriate electronic structure of an electrode is important for multitasking electrocatalytic reactions to achieve higher  $P_{\max}$  and acetoin production. The modeling details related to JF and metal JFs are presented in Figs. S22–S29 and Table S9–S13 (Section 13, Supporting Information). The energy-minimized structures of the JF and metal JF catalysts are shown in Fig. 6a–f. The binding energies were used to investigate metal NP interactions in JF (Table S12). In transition metal atoms, Os ( $-7.90 \text{ eV}$ ) has a higher binding energy toward JF than do other metal nanoclusters because of its high oxophilic nature compared with other metals. The electron density before the metal deposit was chosen to examine the behavior of the electrons in the JF (Fig. 6g). The electron density shows that the  $\text{SiO}_2$  and NCNT parts have sigma and pi bonding electron clouds, respectively. Interestingly, at the  $\text{SiO}_2$ -NCNT interface, the electron cloud delocalization gives the appearance of conductivity.

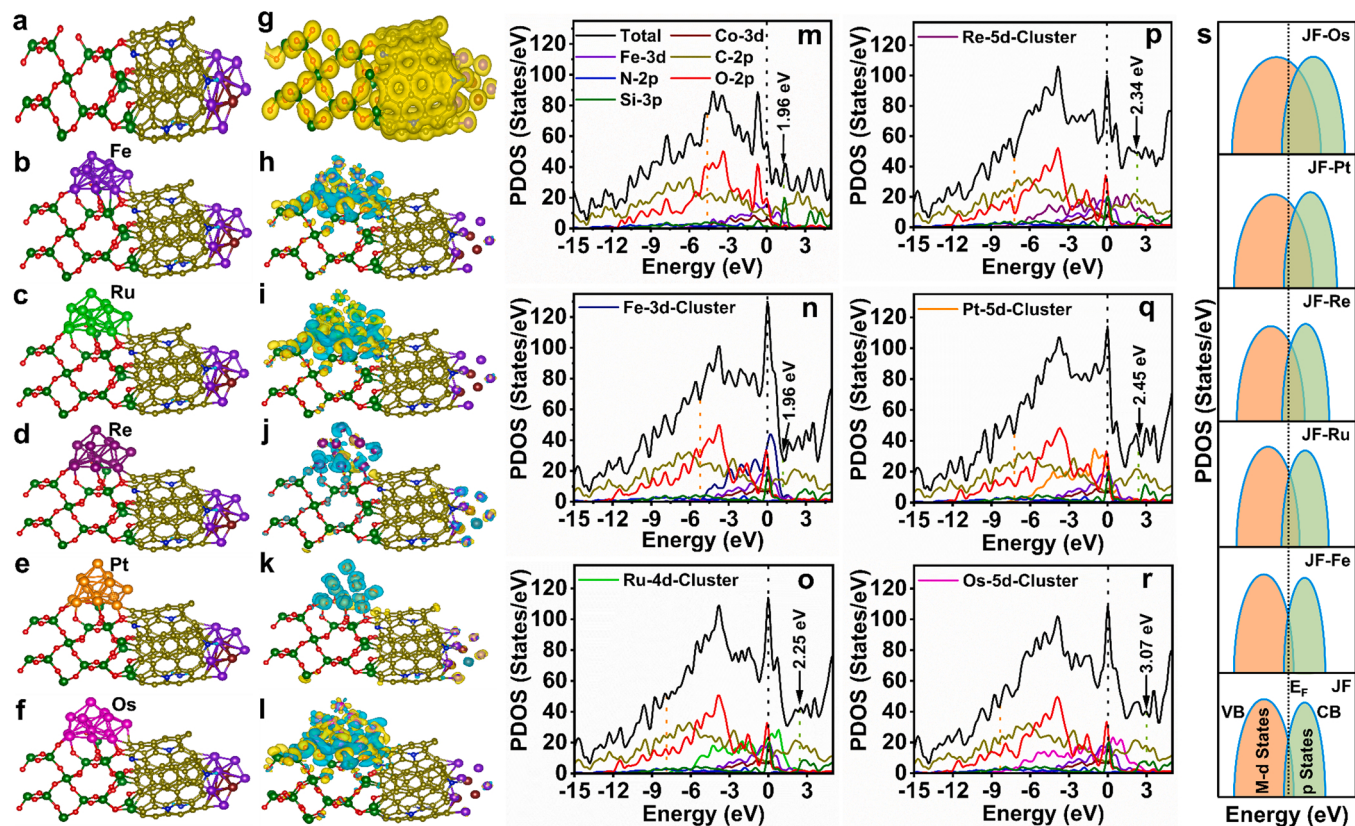


Fig. 6. Energy-minimized structure of a representative model of (a) JF ( $\text{SiO}_2$ -NCNT-CoFe<sub>2</sub>), (b) JF-Fe, (c) JF-Ru, (d) JF-Re, (e) JF-Pt, and (f) JF-Os, (g) electron density contour of the JF with an isosurface value of  $0.06 \text{ e } \text{\AA}^{-3}$  and charge density difference contour of (h) JF-Fe, (i) JF-Ru, (j) JF-Re, (k) JF-Pt, and (l) JF-Os with an isosurface value of  $\pm 0.003 \text{ e } \text{\AA}^{-3}$ . The charge density difference is calculated using the formula  $\nabla\rho = \rho_{\text{Metal+Support}} - \rho_{\text{Metal}} - \rho_{\text{Support}}$ , where  $\nabla\rho$ ,  $\rho_{\text{Metal+Support}}$ ,  $\rho_{\text{Metal}}$ , and  $\rho_{\text{Support}}$  are the charge density difference, the charge density of metal and support, the charge density of metal, and the charge density of support, respectively. In (h–i), the cyan and yellow surfaces are the charge density difference on the surface, indicating the charge reduction ( $\Delta\rho < 0$ ) and coherence ( $\Delta\rho > 0$ ), respectively. Red, blue, dark yellow, olive, gray, wine, and violet are the color codes used to denote oxygen, nitrogen, carbon, silicon, hydrogen, cobalt, and iron, atoms, respectively. Partial density of states plots obtained from the first-principles calculation relative to  $E_F$  of (m) JF, (n) JF-Fe, (o) JF-Ru, (p) JF-Re, (q) JF-Pt, and (r) JF-Os. The dashed lines of black, orange, and (m–r) light green color in visually illustrate the  $E_F$  level, VB maximum level, and CB minimum level, respectively, (s) mechanism illustration of VB (light orange shade) and CB (light green shade) overlap, and d-state delocalization (light yellow shade) around  $E_F$  (dotted line).

While metal nanoparticles interact with JF, the surface electrons present in the metal and JF interact with each other because of the tribo-electrification phenomenon [48–50]. Furthermore, the charge density difference was analyzed to identify the nature of the interface electrons when the metals were in contact with the JF surface. The charge density differences for all metal JFs are depicted in Fig. 6h–l. Assimilation and distortion of the charges are shown in yellow and cyan, respectively. Charge transfer occurs near atoms such as C, N, O, and Si in the  $\text{SiO}_2$ –NCNT interface, which are available for bonding to metal nanoclusters. Charge density difference analysis reveals that all metal atoms have a strong interaction with the support via metal–oxygen, metal–carbon, and metal–silicon bonds. As shown in the figure depicting charge density difference, the metal and nonmetal atoms acquired considerable charge density at the interface compared with the other sites. As shown in the charge density difference of JF–Os (Fig. 6j), interface O concentrates the charge density in the Os–O bond compared with that of other metal JFs, which further facilitates electron transfer.

We estimated the Bader charge at the interface atoms to analyze the electron transfer from metals to JF (Table S13). The Bader charge at the interface atoms in JF–Os is  $-5.87 |\mathbf{q}|$ , which is  $-1.92 |\mathbf{q}|$  higher than that of JF ( $-3.95 |\mathbf{q}|$ ) particles. This excess charge transfer from Os to JF enhanced the electrocatalytic performance. The highly electronegative O atoms in the interface facilitate the abstraction of electrons from the deposited metal nanoparticles. When metal nanoparticles interact with JF particles, their electrons in the occupied (valence band (VB)) and unoccupied (conduction band (CB)) states form newly formed hybrid states subject to hybridization. This newly formed electronic structure has a significant influence on the overall performance of the electrocatalyst.

To dissect this effect at the molecular level, the occupied and unoccupied partial density of states (PDOS) were determined, as depicted in Fig. 6m–r. The Fermi energy level ( $E_F$ ) and PDOS play an indispensable role in the electrocatalytic process for the desired reactions by determining the availability of electrons [51]. For clarity,  $E_F$  was set to 0 eV. The electrocatalytic performance was associated with an overlap between the VB and CB energy states. Connecting the VB to  $E_F$  is favorable for high electron mobility. The PDOS of JF and metal-deposited JFs reveals that the VB is primarily composed of the metal d-state, with a nonmetal p-state contribution. The starting VBs of JF, JF–Fe, JF–Ru, JF–Re, JF–Pt, and JF–Os are  $-4.55$ ,  $-5.14$ ,  $-7.92$ ,  $-7.22$ ,  $-7.17$ , and  $-8.29$  eV to  $E_F$ , respectively (Fig. 6m–r).

The maximum contribution of the d-states in the VB around the  $E_F$  is dominated by the higher energy of the d-states compared with the other orbital energy states. The unoccupied orbitals of Fe, Co, O, C, N, and Si in the deposited metal on the JFs have strong hybrid positions adjacent to  $E_F$ . The appearance of the dominant metal d-states near  $E_F$  confirms the existence of a semimetallic character. After metal deposition, metal d-electrons are found to contribute to the VB by reducing the nonmetal p-states and peak sharpness. Because of the strong hybridization of metal atoms, PDOS becomes wider than pure JF. The intensity gradually decreases from Fe to Os, which is largely caused by metal–support interactions. The VB energy levels of the Fe-deposited JF clusters are similar to those of the control JF because the Fe states in the Fe clusters and  $\text{CoFe}_2$  clusters coalesce and occupy the same position in the VB regime (Fig. 6m). However, an increase in the intensity of the peak was observed in the Fe-deposited JF compared with the control JF because of the increased contribution of Fe d-states. Because of the increase in the effective orbital overlap with the conduction band, the high peak intensity represents the enhanced electrocatalytic activity of JF–Fe compared with JF.

A high d-state delocalization in the CB energy level was observed for the Os (3.07 eV)-deposited JF, whereas other metal-deposited JFs (Fe (1.96 eV), Pt (2.45 eV), Re (2.34 eV), and Ru (2.25 eV)) were found to be lower than those of JF–Os. To elucidate the electronic structure of the catalytic material and investigate the better activity descriptor, the d-state delocalization with unoccupied p-states was considered because it

efficiently overlaps with the VB and CB energy levels around the  $E_F$ . Interestingly, when the deposited metal d-states extend their delocalization from the  $E_F$  along with high-energy CB levels, thus forming new d–p hybrid states, the electron-conducting nature is enhanced. Moreover, d-state delocalization with the CB in metal-deposited JFs (Fig. 6o–r) was considerably shifted compared with that of the JF (Fig. 6m) and directly reflected in the experimental performance, in the order of JF  $<$  JF–Fe  $<$  JF–Ru  $<$  JF–Re  $<$  JF–Pt  $<$  JF–Os. The blueshift of the d-state delocalization position exhibits high catalytic activity because of its highly conducting nature. We drew the density of the state model graph (Fig. 6s) to illustrate the mechanism of d-state delocalization between the VB and CB of deposited metal nanoparticles on JF. Metal deposition can enhance d-state delocalization and semimetallic properties, leading to more populated electrons around  $E_F$ , which facilitates rapid electron transfer. Based on this, new materials with high d-state delocalization can be theoretically screened to further improve the overall electrocatalytic performance. Remarkably, the d-state delocalization of JF–Os is 1.57 times higher than that of JF, and this follows a trend similar to that observed for acetoin production (1.98 times) and power generation (1.93 times) in enzymatic fuel cells.

#### 4. Conclusion

A novel three-dimensional JF-shaped porous nanoparticle ( $\text{SiO}_2$ –NCNT– $\text{CoFe}_2$ ) was synthesized by the scalable spray pyrolysis process, and then used as an anode material in EBFCs. The cascade reaction of EtDH and FLS was applied for the first time in EBFCs for power generation. Simultaneously, the carboligation of EtOH to acetoin without additional cofactors, such as NADH was also reported. The use of the JF–Os–CC–EtDH bioelectrode significantly enhanced the electroenzymatic performance toward EtOH dehydrogenation. This resulted in higher power density with a value of  $1.13 \text{ mW cm}^{-2}$ , which is 4.7-fold higher than plain CC ( $0.24 \text{ mW cm}^{-2}$ ). During co-immobilization, the sequential immobilization of EtDH (93.4% vs. 15.8%) and FLS (92.4% vs. 85.6%) resulted in higher IVs over simultaneous immobilization. JF–Os exhibited a 1.57-fold higher d-state delocalization as compared to JF, thus showing a trend similar to that observed in EBFC for acetoin production (1.98-fold) and power generation (1.93-fold). Thus, the d-state delocalization energy can be a general and reasonable prediction tool for the electrocatalytic performance of EBFCs. This study revealed a variation in power generation depending on the type of metal present on a novel porous JF structure. The power generation recorded a value 37.6 times higher than that of previously reported EBFC processes with DET for EtOH dehydrogenation. Our study provides a novel basis for sustainable power generation from EtOH dehydrogenation with simultaneous value-added chemical production.

#### CRediT authorship contribution statement

All the authors have contributed to the design of experiments, the acquisition and analysis of the experimental data and the writing of the manuscript.

#### Declaration of Competing Interest

The authors declare that they have no known competing financial interests or personal relationships that could have appeared to influence the work reported in this paper.

#### Acknowledgements

This research was supported by Basic Science Research Program through the National Research Foundation of Korea (NRF) funded by the Ministry of Science, ICT & Future Planning (NRF-2021R1A2B5B03002728, NRF-2020R1A4A2002854, 2021M3A9I5023254).

## Appendix A. Supporting information

Supplementary data associated with this article can be found in the online version at [doi:10.1016/j.apcatb.2022.121195](https://doi.org/10.1016/j.apcatb.2022.121195).

## References

- [1] X. Xiao, H.-q. Xia, R. Wu, L. Bai, L. Yan, E. Magner, S. Cosnier, E. Lojou, Z. Zhu, A. Liu, Tackling the challenges of enzymatic (bio)fuel cells, *Chem. Rev.* 119 (2019) 9509–9558, <https://doi.org/10.1021/acs.chemrev.9b00115>.
- [2] I. Mazurenko, X. Wang, A. de Pouliquet, E. Lojou,  $H_2/O_2$  enzymatic fuel cells: from proof-of-concept to powerful device, *Sustain. Energy Fuels* 1 (2017) 1475–1501, <https://doi.org/10.1039/C7SE00180K>.
- [3] C.H. Kwon, Y. Ko, D. Shin, M. Kwon, J. Park, W.K. Bae, S.W. Lee, J. Cho, High-power hybrid biofuel cells using layer-by-layer assembled glucose oxidase-coated metallic cotton fibers, *Nat. Commun.* 9 (2018) 4479, <https://doi.org/10.1038/s41467-018-06994-5>.
- [4] Q. Xu, F. Zhang, L. Xu, P. Leung, C. Yang, H. Li, The applications and prospect of fuel cells in medical field: a review, *Renew. Sustain. Energy Rev.* 67 (2017) 574–580, <https://doi.org/10.1016/j.rser.2016.09.042>.
- [5] C.W. Anson, S.S. Stahl, Mediated fuel cells: soluble redox mediators and their applications to electrochemical reduction of  $O_2$  and oxidation of  $H_2$ , alcohols, biomass, and complex fuels, *Chem. Rev.* 120 (2020) 3749–3786, <https://doi.org/10.1021/acs.chemrev.9b00717>.
- [6] H. Muguruma, H. Iwasa, H. Hidaka, A. Hiratsuka, H. Uzawa, Mediatorless direct electron transfer between flavin adenine dinucleotide-dependent glucose dehydrogenase and single-walled carbon nanotubes, *ACS Catal.* 7 (2017) 725–734, <https://doi.org/10.1021/acscatal.6b02470>.
- [7] I. Mazurenko, A. de Pouliquet, E. Lojou, Recent developments in high surface area bioelectrodes for enzymatic fuel cells, *Curr. Opin. Electrochem.* 5 (2017) 74–84, <https://doi.org/10.1016/j.colelec.2017.07.001>.
- [8] M. Christwardana, Y. Chung, Y. Kwon, A new biocatalyst employing pyrenecarboxaldehyde as an anodic catalyst for enhancing the performance and stability of an enzymatic biofuel cell, *NPG Asia Mater.* 9 (2017), e386, <https://doi.org/10.1038/am.2017.75>.
- [9] M. Christwardana, Y. Chung, Y. Kwon, Co-immobilization of glucose oxidase and catalase for enhancing the performance of a membraneless glucose biofuel cell operated under physiological conditions, *Nanoscale* 9 (2017) 1993–2002, <https://doi.org/10.1039/C6NR09103B>.
- [10] D. Majdecka, S. Draminska, D. Janusek, P. Krysinski, R. Bilewicz, A self-powered biosensing device with an integrated hybrid biofuel cell for intermittent monitoring of analytes, *Biosens. Bioelectron.* 102 (2018) 383–388, <https://doi.org/10.1016/j.bios.2017.11.045>.
- [11] M. Liu, R. Zhang, W. Chen, Graphene-supported nanoelectrocatalysts for fuel cells: synthesis, properties, and applications, *Chem. Rev.* 114 (2014) 5117–5160, <https://doi.org/10.1021/cr400523y>.
- [12] Y. Zhou, Z. Zhou, R. Shen, R. Ma, Q. Liu, G. Cao, J. Wang, Correlating electrocatalytic oxygen reduction activity with d-band centers of metallic nanoparticles, *Energy Storage Mater.* 13 (2018) 189–198, <https://doi.org/10.1016/j.ensm.2018.01.011>.
- [13] J. Galindo-de-la-Rosa, N. Arjona, A. Moreno-Zuria, E. Ortiz-Ortega, M. Guerra-Balcázar, J. Ledesma-García, L.G. Arriaga, Evaluation of single and stack membraneless enzymatic fuel cells based on ethanol in simulated body fluids, *Biosens. Bioelectron.* 92 (2017) 117–124, <https://doi.org/10.1016/j.bios.2017.02.010>.
- [14] K.-N.T. Tseng, S. Lin, J.W. Kampf, N.K. Szymczak, Upgrading ethanol to 1-butanol with a homogeneous air-stable ruthenium catalyst, *Chem. Commun.* 52 (2016) 2901–2904, <https://doi.org/10.1039/C5CC09913G>.
- [15] J.H. Franco, S.A. Neto, D.P. Hickey, S.D. Minteer, A.R. de Andrade, Hybrid catalyst cascade architecture enhancement for complete ethanol electrochemical oxidation, *Biosens. Bioelectron.* 121 (2018) 281–286, <https://doi.org/10.1016/j.bios.2018.09.011>.
- [16] L. Zhang, R. Singh, S. D, Z. Guo, J. Li, F. Chen, Y. He, X. Guan, Y.C. Kang, J.-K. Lee, An artificial synthetic pathway for acetoate, 2,3-butanediol, and 2-butanol production from ethanol using cell free multi-enzyme catalysis, *Green Chem.* 20 (2018) 230–242, <https://doi.org/10.1038/am.2017.7510.1039/C7GC02898A>.
- [17] Emolecules, Acetoin Price, 2021,
- [18] T. Werpy, G. Petersen, Top value added chemicals from biomass: volume I—results of screening for potential candidates from sugars and synthesis gas, *Natl. Renew. Energy Lab.* (2004), <https://doi.org/10.2127/15008895>.
- [19] G.D. Park, J.-K. Lee, Y.C. Kang, Synthesis of uniquely structured  $SnO_2$  hollow nanoplates and their electrochemical properties for Li-ion storage, *Adv. Funct. Mater.* 27 (2017), 1603399, <https://doi.org/10.1002/adfm.201603399>.
- [20] W. Li, D. Zhao, Extension of the Stöber method to construct mesoporous  $SiO_2$  and  $TiO_2$  shells for uniform multifunctional core–shell structures, *Adv. Mater.* 25 (2013) 142–149, <https://doi.org/10.1002/adma.201203547>.
- [21] J. Wang, S. Kaskel, KOH activation of carbon-based materials for energy storage, *J. Mater. Chem.* 22 (2012) 23710–23725, <https://doi.org/10.1039/C2JM34066F>.
- [22] S. Kondaveeti, S.-H. Lee, H.-D. Park, B. Min, Specific enrichment of different *Geobacter* sp. in anode biofilm by varying interspatial distance of electrodes in air-cathode microbial fuel cell (MFC), *Electrochim. Acta* 331 (2020), 135388, <https://doi.org/10.1016/j.electacta.2019.135388>.
- [23] P. Giannozzi, S. Baroni, N. Bonini, M. Calandra, R. Car, C. Cavazzoni, D. Ceresoli, G.L. Chiarotti, M. Cococcioni, I. Dabo, A. Dal Corso, S. de Gironcoli, S. Fabris, G. Fratesi, R. Gebauer, U. Gerstmann, C. Gougaudis, A. Kokalj, M. Lazzeri, L. Martin-Samios, N. Marzari, F. Mauri, R. Mazzarello, S. Paolini, A. Pasquarello, L. Paulatto, C. Sbraccia, S. Scandolo, G. Scalzaro, A.P. Seitsonen, A. Smogunov, P. Umari, R.M. Wentzcovitch, QUANTUM ESPRESSO: a modular and open-source software project for quantum simulations of materials, *J. Phys. Condens. Matter* 21 (2009), 395502, <https://doi.org/10.1088/0953-8984/21/39/395502>.
- [24] G.M. Morris, R. Huey, W. Lindstrom, M.F. Sanner, R.K. Belew, D.S. Goodsell, A. J. Olson, AutoDock4 and AutoDockTools4: automated docking with selective receptor flexibility, *J. Comput. Chem.* 30 (2009) 2785–2791, <https://doi.org/10.1002/jcc.21256>.
- [25] H.-S. Lu, H. Zhang, R. Liu, X. Zhang, H. Zhao, G. Wang, Macroscale cobalt-MOFs derived metallic Co nanoparticles embedded in N-doped porous carbon layers as efficient oxygen electrocatalysts, *Appl. Surf. Sci.* 392 (2017) 402–409, <https://doi.org/10.1016/j.apsusc.2016.09.045>.
- [26] H. Ali-Löytty, M.W. Louie, M.R. Singh, L. Li, H.G. Sanchez Casalongue, H. Ogasawara, E.J. Crumlin, Z. Liu, A.T. Bell, A. Nilsson, D. Friebel, Ambient-pressure XPS study of a Ni–Fe electrocatalyst for the oxygen evolution reaction, *J. Phys. Chem. C* 120 (2016) 2247–2253, <https://doi.org/10.1021/acs.jpcscb.5b10931>.
- [27] A. Pitto-Barry, L.M.A. Perdigao, M. Walker, J. Lawrence, G. Costantini, P.J. Sadler, N.P.E. Barry, Synthesis and controlled growth of osmium nanoparticles by electron irradiation, *Dalton Trans.* 44 (2015) 20308–20311, <https://doi.org/10.1039/C5DT03205A>.
- [28] T.M. David, K.I. Gnanasekar, P. Wilson, P. Sagayaraj, T. Mathews, Effect of Ni, Pd, and Pt nanoparticle dispersion on thick films of  $TiO_2$  nanotubes for hydrogen sensing: TEM and XPS studies, *ACS Omega* 5 (2020) 11352–11360, <https://doi.org/10.1021/acsomega.0c00292>.
- [29] J. Okal, W. Tylus, L. Kępiński, XPS study of oxidation of rhenium metal on  $\gamma-Al_2O_3$  support, *J. Catal.* 225 (2004) 498–509, <https://doi.org/10.1016/j.jcat.2004.05.004>.
- [30] S. Akbayrak, S. Özkar, Ruthenium(0) nanoparticles supported on multiwalled carbon nanotube as highly active catalyst for hydrogen generation from ammonia–borane, *ACS Appl. Mater. Interfaces* 4 (2012) 6302–6310, <https://doi.org/10.1021/am3019146>.
- [31] Y. Mao, H. Duan, B. Xu, L. Zhang, Y. Hu, C. Zhao, Z. Wang, L. Chen, Y. Yang, Lithium storage in nitrogen-rich mesoporous carbon materials, *Energy Environ. Sci.* 5 (2012) 7950–7955, <https://doi.org/10.1039/C2EE21817H>.
- [32] D. Su, M. Cortie, G. Wang, Fabrication of N-doped graphene–carbon nanotube hybrids from prussian blue for lithium–sulfur batteries, *Adv. Energy Mater.* 7 (2017), 1602014, <https://doi.org/10.1002/aenm.201602014>.
- [33] Y.-J. Shih, M.-S. Wu, Nitrogen-doped and reduced graphene oxide scrolls derived from chemical exfoliation of vapor-grown carbon fibers for electrochemical supercapacitors, *Electrochim. Acta* 353 (2020), 136503, <https://doi.org/10.1016/j.electacta.2020.136503>.
- [34] M. Thommes, K. Kaneko, A.V. Neimark, J.P. Olivier, F. Rodriguez-Reinoso, J. Rouquerol, K.S. Sing, Physiorption of gases, with special reference to the evaluation of surface area and pore size distribution (IUPAC Technical Report), *Pure Appl. Chem.* 87 (2015) 1051–1069, <https://doi.org/10.1515/pac-2014-1117>.
- [35] S.K. Kuk, Y. Ham, K. Gopinath, P. Boonmongkolras, Y. Lee, Y.W. Lee, S. Kondaveeti, C. Ahn, B. Shin, J.-K. Lee, S. Jeon, C.B. Park,  $CO_2$  reduction: continuous 3D titanium nitride nanoshell structure for solar-driven unbiased biocatalytic  $CO_2$  reduction (Adv. Energy Mater. 25/2019), *Adv. Energy Mater.* 9 (2019), 1970097, <https://doi.org/10.1002/aenm.201970097>.
- [36] F. Ran, Y. Zou, Y. Xu, X. Liu, H. Zhang, Fe3O4@MoS2@PEI-facilitated enzyme tethering for efficient removal of persistent organic pollutants in water, *Chem. Eng. J.* 375 (2019), 121947, <https://doi.org/10.1016/j.cej.2019.121947>.
- [37] B. Peng, C. Takai, H. Razavi-khosroshahi, M. Fujii, Effect of silane modification on CNTs/silica composites fabricated by a non-firing process to enhance interfacial property and dispersibility, *Adv. Powder Technol.* 29 (2018) 2091–2096, <https://doi.org/10.1016/j.apt.2018.05.017>.
- [38] Y. Chung, J. Ji, Y. Kwon, Performance evaluation of enzymatic biofuel cells using a new cathodic catalyst containing hemin and poly acrylic acid promoting the oxygen reduction reaction, *J. Mater. Chem. C* 7 (2019) 11597–11605, <https://doi.org/10.1039/C9TC03071A>.
- [39] A. Sobolikina, V. Mechteleherine, C. Bellmann, V. Khavrus, S. Oswald, S. Hampel, A. Leonhardt, Surface properties of CNTs and their interaction with silica, *J. Colloid Interface Sci.* 413 (2014) 43–53, <https://doi.org/10.1016/j.jcis.2013.09.033>.
- [40] D. Ivynski, K. Artyushkova, R.A. Rincón, P. Atanassov, H.R. Luckarift, G. R. Johnson, Entrapment of enzymes and carbon nanotubes in biologically synthesized silica: glucose oxidase-catalyzed direct electron transfer, *Small* 4 (2008) 357–364, <https://doi.org/10.1002/smll.200700725>.
- [41] B.-R. Adhikari, H. Schraft, A. Chen, A high-performance enzyme entrapment platform facilitated by a cationic polymer for the efficient electrochemical sensing of ethanol, *Analyst* 142 (2017) 2595–2602, <https://doi.org/10.1039/C7AN00594F>.
- [42] T. Yakushi, K. Matsushita, Alcohol dehydrogenase of acetic acid bacteria: structure, mode of action, and applications in biotechnology, *Appl. Microbiol. Biotechnol.* 86 (2010) 1257–1265, <https://doi.org/10.1007/s00253-010-2529-z>.
- [43] J. Tang, R.M.L. Werchmeister, L. Preda, W. Huang, Z. Zheng, S. Leimkühler, U. Wollenberger, X. Xiao, C. Engelbrekt, J. Ulstrup, J. Zhang, Three-dimensional sulfite oxidase bioanodes based on graphene functionalized carbon paper for sulfite/O<sub>2</sub> biofuel cells, *ACS Catal.* 9 (2019) 6543–6554, <https://doi.org/10.1021/acscatal.9b01715>.

- [44] X. Wang, T. Saba, H.H.P. Yiu, R.F. Howe, J.A. Anderson, J. Shi, Cofactor NAD(P)H regeneration inspired by heterogeneous pathways, *Chem* 2 (2017) 621–654, <https://doi.org/10.1016/j.chempr.2017.04.009>.
- [45] G. Awad, E.F. Mohamed, Immobilization of P450 BM3 monooxygenase on hollow nanosphere composite: Application for degradation of organic gases pollutants under solar radiation lamp, *Appl. Catal. B* 253 (2019) 88–95, <https://doi.org/10.1016/j.apcatb.2019.04.045>.
- [46] Heraeus, Osmium(III) Chloride Heraeus Precious Metals, Hanau, Germany, 2021.
- [47] J. Roether, K.-Y. Chu, N. Willenbacher, A.Q. Shen, N. Bhalla, Real-time monitoring of DNA immobilization and detection of DNA polymerase activity by a microfluidic nanoplasmonic platform, *Biosens. Bioelectron.* 142 (2019), 111528, <https://doi.org/10.1016/j.bios.2019.111528>.
- [48] E. Solessio, G.A. Engbretson, Antagonistic chromatic mechanisms in photoreceptors of the parietal eye of lizards, *Nature* 364 (1993) 442–445, <https://doi.org/10.1038/364442a0>.
- [49] J. Lowell, A.C. Rose-Innes, Contact electrification, *Adv. Phys.* 29 (1980) 947–1023, <https://doi.org/10.1080/00018738000101466>.
- [50] J.A. Wiles, M. Fialkowski, M.R. Radowski, G.M. Whitesides, B.A. Grzybowski, Effects of surface modification and moisture on the rates of charge transfer between metals and organic materials, *J. Phys. Chem. B* 108 (2004) 20296–20302, <https://doi.org/10.1021/jp0457904>.
- [51] B. Hammer, J.K. Nørskov, Theoretical surface science and catalysis—calculations and concepts, *Adv. Catal.* 45 (2000) 71–129.